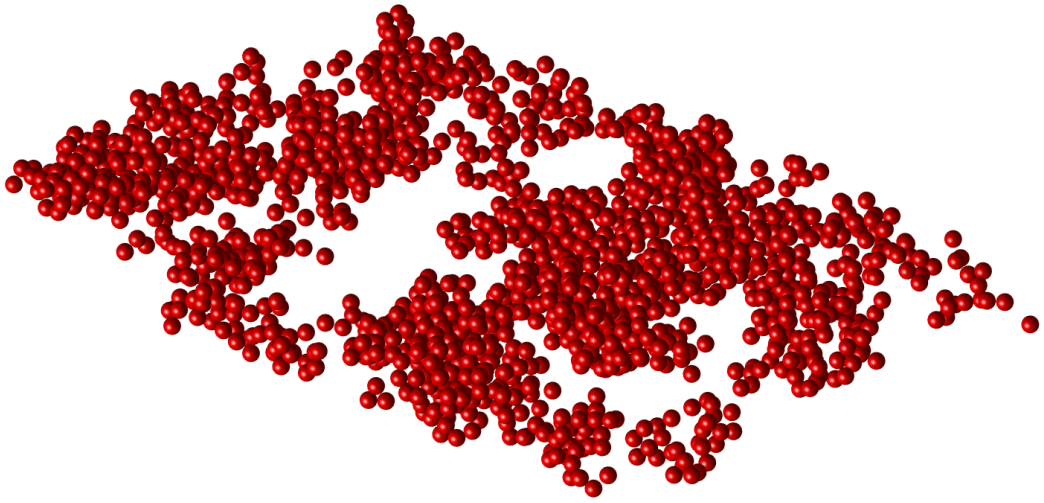


Spatial Modeling of Formation of Gel

A simulation study to investigate aggregatation dynamics of colloidal silica

Master's thesis in Engineering Mathematics and Computational Science

Jakob Antonsson

Department of Mathematical Sciences
CHALMERS UNIVERSITY OF TECHNOLOGY
Gothenburg, Sweden 2022
www.chalmers.se

Master's thesis 2022

Spatial Modeling of Formation of Gel

A simulation study to investigate aggregatation dynamics of colloidal silica

Jakob Antonsson



CHALMERS
UNIVERSITY OF TECHNOLOGY

Department of Mathematical Sciences
Division of Applied Mathematics and Statistics
Chalmers University of Technology
Gothenburg, Sweden 2022

Spatial Modeling of Formation of Gel
A simulation study to investigate aggregation dynamics of colloidal silica
Jakob Antonsson

© JAKOB ANTONSSON, 2022.

Supervisor: Aila Särkkä, Depertment of Mathematical Sciences
Examiner: Tobias Gebäck, Department of Mathematical Sciences

Master's Thesis 2022
Department of Mathematical Sciences
Division of Applied Mathematics and Statistics
Chalmers University of Technology
SE-412 96 Gothenburg

Typeset in LaTeX
Printed by Chalmers Reproservice
Gothenburg, Sweden 2022

Spatial Modeling of Formation of Gel
A simulation study to investigate aggregation dynamics of colloidal silica
Jakob Antonsson
Department of Mathematical Sciences
Chalmers University of Technology

Abstract

Understanding and predicting colloidal interaction is important in a variety of applications. In this study, we investigate aggregation dynamics of colloidal silica by generating simulated structures and comparing them to experimental data gathered through scanning transmission electroscopy (STEM). More specifically, diffusion-limited cluster aggregation (DLCA) and reaction-limited cluster aggregation (RLCA) models with different functions for the probability of particles sticking upon contact were used. Aside from using a constant sticking probability, the sticking probability was allowed to depend on the masses of the colliding clusters and on the number of particles close to the collision. It was found that in comparison to using a constant sticking probability, both the mass-dependent and neighbor-dependent sticking probability improved the goodness-of-fit of spatial summary statistics when the simulated data were compared to the experimental data. The models were also compared based on fractal dimensions. Both in terms of goodness-of-fit for the summary statistics and the fractal dimension, the structures generated with a neighbor-dependent sticking probability were the most similar to the experimental data. This model was further analyzed by conducting global envelope tests based on the spatial summary statistics. The tests showed that although the summary statistics are similar for the simulated and experimental structures, there are also systematic deviations. Structures generated with the same model were also compared with the STEM data by simulating flow and diffusion. From this analysis, it was seen that the permeability and the geometry factor of the simulated and experimental structures were relatively similar.

Acknowledgements

I am very grateful to my supervisor **Aila Särkkä** for her help and continuous support during the writing of this thesis. Thank you for regularly taking the time to discuss and provide feedback on the project. I would also like to thank my examiner **Tobias Gebäck** for helping me with the simulation code and for giving me advice on how to use the Gesualdo software. In addition, I would like to thank **Charlotte Hamngren Blomqvist** for providing me with her Ph.D. thesis and answering my questions on how the experimental data was gathered.

Jakob Antonsson, Gothenburg 2022

Contents

List of Figures **xi**

List of Tables **xiii**

1 Introduction **1**

2 Colloidal Silica and Experimental Data **3**
2.1 Silica hydrogel . . . 3
2.2 Experimental data . . . 4

3 Cluster aggregation models **5**
3.1 Brownian motion and diffusion . . . 5
3.2 DLVO theory and Smoluchowski coagulation equation . . . 6
3.3 DLCA and RLCA models . . . 7
3.4 Distribution of particle diameter . . . 8
3.5 Models for sticking probability . . . 8
3.5.1 Constant sticking probability . . . 9
3.5.2 Sticking probability dependent on cluster size . . . 9
3.5.3 Sticking probability dependent on particles close to collision . 10
3.6 Implementation . . . 11

4 Model Evaluation **13**
4.1 Spatial Point Processes . . . 13
4.1.1 Basic Definitions . . . 13
4.1.1.1 Point Process . . . 13
4.1.1.2 Notation . . . 14
4.1.1.3 Distributions . . . 14
4.1.1.4 Stationarity and Isotropy . . . 15
4.1.1.5 Intensity measure and intensity . . . 15
4.1.2 Summary Statistics . . . 15
4.1.2.1 Empty Space Function . . . 16
4.1.2.2 L-function . . . 16
4.1.2.3 Clustering function . . . 17
4.1.2.4 Mean cluster size function . . . 18
4.1.3 Evaluation of models based on functional summary statistics . 19
4.1.3.1 Parameter selection . . . 19
4.1.3.2 Global envelope test . . . 20

4.1.4 Computational tools 20
4.2 Fractal scaling properties 21
4.3 Mass transport 21
4.3.1 Flow 21
4.3.2 Diffusion 23
4.3.3 Software 23

5 Results **25**
5.1 Goodness of fit for summary statistics 25
5.1.1 Constant sticking probability 25
5.1.2 Mass dependent sticking probability 27
5.1.3 Sticking probability dependent on the number of particles close to collision 29
5.1.4 Global envelope tests 31
5.2 Fractal dimension 35
5.3 Mass transport properties 35
5.3.1 Flow 35
5.3.2 Diffusion 38

6 Conclusions and suggestions for further research **41**

Bibliography **45**

List of Figures

2.1 Geometrical representation of the experimental data where all particles have been assumed to have a diameter of 21 nm. 4

3.1 Histogram of nearest neighbor distances from the experimental data and the estimated probability density function of particle diameters. . 9
3.2 Illustration of how the sticking probability in equation 3.14 is calculated. 11

4.1 The observational window W and the eroded window $W_{\ominus,r}$, which is shaded in grey. We can see that for points in $W \backslash W_{\ominus,r}$ there is the possibility that points have neighbors at distances smaller than r that we do not observe. 18
4.2 Illustration of the normal box counting procedure to the left and the random box counting on the right. 22

5.1 Total sum of squares from simulations with model 1. 26
5.2 Pooled averages for the four summary statistics from simulation with a constant sticking probability $p = 0.0001$ (green) and from the STEM-data (black). 26
5.3 Total sum of squares S from simulations with model 2 (blue) and corresponding value of S from model 1 with $p = p_0$ (orange). 28
5.4 Pooled averages for the four summary statistics from simulation with a mass-dependent sticking probability with $p_0 = 0.01$ and $\sigma = -0.25$, and from the STEM-data (black). 28
5.5 Total sum of squares S from simulations with model 2 (blue) and corresponding value of S from model 1 with $p = p_0$ (orange). 30
5.6 Pooled averages for the four summary statistics from simulating with model 3 with $p_0 = 0.0001$, $\delta = 0.001$ and $d = 2.5$, and from the STEM-data (black). 31
5.7 Global envelope test for the empty space function. The grey band is the envelope, whereas the dashed line is the central function from the simulations. The black curve corresponds to the STEM data. 32
5.8 Global envelope test for the centered L-function. The black curve corresponds to the STEM data. 33
5.9 Global envelope for the clustering function. The black curve corresponds to the STEM data. 34

5.10 Global envelope for the mean cluster size function. The black curve corresponds to the STEM data. 34
5.11 Flow simulation for the experimental gel in the Y direction. 37
5.12 Flow simulation in the Y-direction for the gel with permeability closest to the average permeability of the simulated gels. 38

List of Tables

3.1 Every row contains the values of p_0 and σ that have been tried in combination when simulating with model 2. 10

5.1 Parameters that correspond to the different indices in figure 5.1 . . . 26
5.2 Parameters that correspond to the different indices in figure 5.3 . . . 28
5.3 Parameters that correspond to the different indices in figure 5.5. . . . 30
5.4 Estimated fractal dimensions D_f with standard error (SE) from linear regression. 35
5.5 Table of the calculated permeability from flow simulations in two different directions. The average permeability from the 5 simulated structures is denoted by $\overline{\kappa}_{\text{sim}}$, whereas the minimum and maximum out of these permeabilities is denoted by $\kappa_{\text{sim}}^{\text{min}}$ and $\kappa_{\text{sim}}^{\text{max}}$. 36
5.6 The geometry factor from the diffusion simulations in two different directions. The average of the geometry factor from the 5 simulated structures is denoted by $\overline{G}_{\text{sim}}$, whereas the minimum and maximum out is denoted by $G_{\text{sim}}^{\text{min}}$ and $G_{\text{sim}}^{\text{max}}$. 39

1
Introduction

The study of colloidal interaction is relevant in many applications areas, such as food processing, battery science and pharmacology. For instance, prediction of colloidal aggregation is often important in target drug delivery systems [1]. In this project, different 3D models for aggregation of silica nanoparticles are investigated by comparing simulated post-aggregated structures with data from experiments. Colloidal silicas are suspensions of typically nearly spherical silica nanoparticles in a liquid phase, and such a suspension can turn into a gel through aggregation of the silica particles. Silica gels are of great use for studying colloidal aggregation since various structures can be obtained.

In Häbel *et al.* (2019), silica particle aggregation was studied in 3D by comparing an experimentally obtained aggregate to simulated structures [1]. The aggregation was simulated using diffusion-limited cluster aggregation (DLCA) and reaction-limited cluster aggregation (RLCA) models. In DLCA and RLCA, particles follow Brownian motion, but the models differ in the probability of particles aggregating upon collision. To analyze the models, Häbel *et al.* looked at the goodness-of-fit of spatial summary functions. In their simulations, all primary particles had a diameter of 20 nm, but they noticed variations in the diameter in the experimental gel structure. Lovisa Köllerström followed up on this in her Master Thesis (2020) [2] and performed simulations with particles of different sizes. This led to an improvement in the goodness-of-fit of the summary statistics, but there is still interest in further development.

This thesis investigates different functions for the probability of particles and clusters sticking upon contact. This will be referred to as the *sticking probability*. More specifically, models involving the mass of the clusters and interaction with multiple particles at the collision site are tested. The comparison of simulated structures and data from experiments consists of comparing the structural resemblance through spatial summary statistics, fractal scaling, and mass transport properties.

2

Colloidal Silica and Experimental Data

In this chapter, some main characteristics of silica hydrogels and how they are formed are presented. Furthermore, the experiment conducted to gather the data used in this study is briefly laid out along with some properties of the data set.

2.1 Silica hydrogel

A *gel* is a semi-solid material composed of microscopic subunits, for instance, nanoparticles, which bind to each other and form a continuous network in a liquid medium. The nanoparticles comprising the network are sometimes also called *primary particles*. Two main types of gels are *physical* and *chemical gels*, in which the internal network is held together by physical forces and chemical bonds, respectively. In the case of amorphous silicon dioxide (SiO_2), the silica nanoparticles are bound to each other through covalent bonds. Therefore, it is a type of chemical gel. If the nanoparticles are not bound to each other but are merely suspended in a solvent, we call it a *sol*. It is important to distinguish this from a solution where the particles dissolve into single molecules/ions in the solvent [3]. The surface of amorphous silica is the silanol group ($\equiv Si - OH$) and siloxane group ($\equiv SiO_2$). However, the silanol group is not very important for the surface characteristics discussed in this thesis since they are chemically inactive in most industrially produced silica sols [3]. The silanol group can become negatively charged through the reaction $SiOH \Leftrightarrow SiO^- + H^+$ for pH in the range from the *point of zero charge* (PZC) to 12. The PZC is the pH at which the net surface charge equals 0. This kind of deprotonation will lead to silica nanoparticles carrying a negative surface charge since the charge can become stabilized through hydrogen bonds between neighboring groups. For most industrially produced silica sols, this is the main factor of stabilization when pH is above the PZC, since the electromagnetic repulsion between silica particles hinders aggregation.

In order to induce aggregation in silica, the most common method in industry is to add cations to the sol. The cations are attracted to the silica particles' negative surfaces and reduce the surface charge. Consequently, the repulsive electromagnetic forces are diminished, and at a critical concentration of ions, the formation of a silica hydrogel starts. The time it takes for the gel to form can be controlled by the concentration of ions in the solvent, where a higher concentration gives rise to less

repulsion between the particles and a quicker gel time.

2.2 Experimental data

No physical experiments were carried out as a part of this thesis; however, the simulated silica hydrogels were compared to data consisting of positions of the centroids of silica particles in an experimentally created silica hydrogel. The data had already been imaged, preprocessed, and analyzed in earlier studies. This section contains a brief description of the experiments to understand the data that has been used. More detailed explanations of the experiments and the estimation of the particle centroids can be found in Hamngren Blomqvist (2016) [4].

The gel was created from a colloidal silica sol (Bindzil 40/130), provided by AkzoNobel, with a 42.3 wt% silica concentration. The suspension's pH was lowered by adding NaCl and using ion exchange pearls that were removed after use with suction filtration. Ultra-pure deionized water and NaCl was added to the filtered sol resulting in a 9 wt% concentration of silica. The NaCl concentration was then adjusted to 0.5 M and the pH to 7.8 before the mixture was vortexed and left to gel for one day.

After the gelation had finished, a sample of an inner part of the gel was extracted and cut into thin slices between 70 and 300 nm thick. These slices were then imaged using high angle annular dark field (HAADF) scanning transmission electron microscopy (STEM). By using tools from image analysis, a binary image separating particles and void was generated. The particle centroids were estimated from this image by using a maximum-likelihood approach. In the sample that has been studied in this project, 1699 particles were found in an observational window of size $740 \times 1075 \times 100$ nm^3. A geometrical representation of the data can be found in figure 2.1.

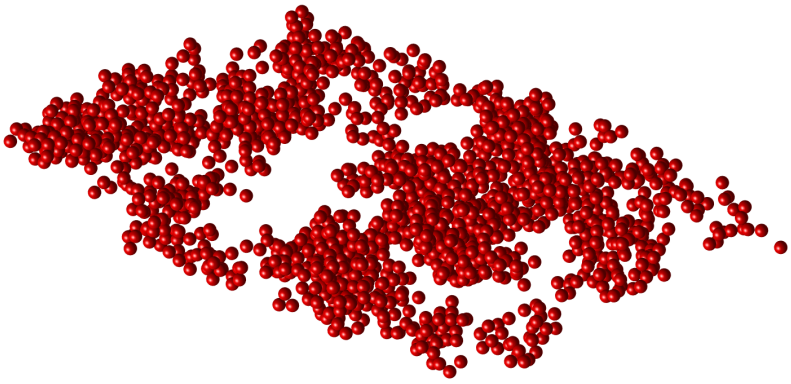


Figure 2.1: Geometrical representation of the experimental data where all particles have been assumed to have a diameter of 21 nm.

3

Cluster aggregation models

In the following sections, the models used to simulate particle aggregation are introduced.

3.1 Brownian motion and diffusion

Industrially produced silica sols often contain particles smaller than 100 nm. The main movement of such particles can be modeled as a random walk behaviour driven by thermal energy in the system [3]. The motion of particles can be assumed to follow *Brownian motion* or a *Wiener process* $\{W(t)\}_{t\geq 0}$. A one-dimensional Wiener process W is a stochastic process that fulfills the following conditions [5]:

- $W(0) = 0$.
- The process W has stationary and independent increments, i.e. if $r < s \leq t < u$ then $W(u) - W(t)$ and $W(s) - W(r)$ are independent stochastic variables.
- For $s < t$ the stochastic variable $W(t) - W(s)$ has normal distribution $N[0, \sigma^2(t - s)]$.
- W has continuous trajectories.

In a multidimensional setting, we define a standard d-dimensional Weiner process as a vector-valued stochastic process

$$W(t) = [W^{(1)}(t), W^{(2)}(t), \ldots, W^{(d)}(t)] \tag{3.1}$$

where the components are independent standard one-dimensional Wiener processes.

The Wiener process gives us a microscopic description of how a single particle moves under diffusion. A macroscopic representation is instead given by the diffusion equation [6]. Let us consider a monodisperse system where all particles have the same diffusion coefficient, and the surrounding medium is homogeneous. The diffusion equation is a partial differential equation (PDE) of the form:

$$\frac{\partial \varphi(x,t)}{\partial t} = D\nabla^2 \varphi(x,t) \tag{3.2}$$

and describes how the concentration $\varphi(x,t)$ which depends on location $x \in \mathbb{R}^3$ and time $t \in [0,\infty)$ changes with respect to time. The coefficient $D > 0$ is called the diffusion coefficient, and ∇^2 is the Laplace operator. If we solve equation 3.2 for a total of n particles which are all located at the origin at $t = 0$ we get the unique solution

$$\varphi_0(x,t) = \frac{n}{\sqrt{4\pi Dt}} \exp\left(-\frac{x^2}{4Dt}\right).$$

(3.3)

Hence, the concentration of particles is a gaussian function around the initial positions of the particles with variance proportional to the time passed. There is a natural connection between this representation and that of the Weiner process since the transition probability

$$P(W(t) \in dx | W(0) = 0) = \frac{1}{n}\varphi_0(x,t) \tag{3.4}$$

for a Wiener process with $\sigma = 2D$.

3.2 DLVO theory and Smoluchowski coagulation equation

The physicochemical forces during the aggregation of silica are complex. As a consequence, simplified models have been proposed. Among the more prominent models is the Derjaguin-Landau-Verwey-Overbeek (DLVO) theory, in which the interaction between particles is assumed to only consist of electrostatic repulsion and London-van der Waals attraction [7]. The London-van der Waals interaction energy is given by

$$V_{\text{att}} = -\frac{A}{12} H(d,r) \tag{3.5}$$

where A is the Hamaker constant and $H(d,r)$ is the Hamaker function dependent on the interparticle distance and particle radius. The Hamaker constant of silica is smaller than what is typical for other electrostatic colloidal oxides such as titanium dioxide TiO_2. For instance, the Hamaker constant of silica has been found to be about 35 times smaller than that of TiO_2 for particles of the same size. Consequently, the attraction energy is not as strongly dominated by the London-van der Waals interaction in the case of silica. Experiments have shown that other short-range forces, known as structural forces, play an important role in the interaction process [8]. In addition, the DLVO theory only considers the interaction between pairs of single particles and not clusters [7]. It has therefore been difficult to satisfactorily explain the behaviour of colloidal silica using only the DLVO theory.

An earlier and more general attempt at modeling aggregation kinetics was developed by Smolushowski and describes how the distribution of cluster masses develops in

time [9]. In the case when the masses of the aggregates are continuous variables, the number of clusters $n(m,t)$ with mass m at time t evolves as

$$\frac{\partial n(m,t)}{\partial t} = \frac{1}{2}\int_0^m K(x, m-x)n(x,t)n(m-x,t)\,\mathrm{d}x - \int_0^m K(m,x)n(m,t)n(x,t)\,\mathrm{d}x. \tag{3.6}$$

An important part of the model is the coagulation kernel $K(m_1, m_2)$ which describe the rate at which clusters of mass m_1 and m_2 form clusters of mass $m_1 + m_2$. For certain functional forms of the coagulation kernel, the Smoluchowski coagulation equation can be solved analytically for the DLCA and RLCA models presented below. The Smoluchowski coagulation equation has not been used directly in this project; however, studies investigating the development of cluster masses for DLCA and RLCA models will be relevant for discussing our results.

3.3 DLCA and RLCA models

In both *diffusion-limited cluster aggregation* (DLCA) and *reaction-limited cluster aggregation* (RLCA) models, the particles are assumed to follow Brownian motion due to diffusion. The Brownian particles only interact with one another upon collision, at which they have some probability of sticking together. In DLCA, all collisions lead to the particles sticking together and diffusing as a cluster, whereas in RLCA, the sticking probability is smaller than 1.

The DLCA regime corresponds to a scenario where repulsive mechanisms between clusters can be neglected. Since the main reason for the repulsion between clusters is electromagnetic repulsion, this model has been considered more applicable in cases when the concentration of ions is high in the surrounding solvent [3]. Reversely, when the ionic concentration is low, aggregates will be formed to reduce the surface energy by having fewer surface groups. This gives rise to more compact clusters, which is the case for RLCA models since particles can penetrate deeper into clusters before sticking to them.

Clusters formed through DLCA and RLCA have been found to have fractal properties. One consequence of this fractal morphology is that the mass of an aggregate m_{cl} scales with the radius of gyration R_g according to

$$m_{cl} \propto R_g^{D_f} \tag{3.7}$$

where D_f is the mass fractal dimension, which will be referred to as simply the fractal dimension from this point onward. The fractal dimension D_f is often used as a fundamental description of the morphology of an aggregate. It provides a quantitative measure of the degree to which a structure fills the physical space [10]. In three-dimensional Euclidean space, the values of D_f can range from 1-3. A fractal dimension of 1 corresponds to a line, 2 to a plane and 3 to a cube.

As mentioned earlier, structures formed through RLCA will, in general, be denser compared to DLCA, and as a consequence, the fractal dimension is higher for RLCA

than DLCA. In three dimensions, the values of the fractal dimensions have been found to typically vary between $1.7 - 1.8$ for DLCA and $1.9 - 2.1$ for RLCA. However, the fractal dimension also depends on the concentration and the sizes of the primary particles [11].

The mobility of a cluster in DLCA and RLCA simulations depends on its mass. In particular, the diffusion coefficient D_{cl} of a cluster with mass m_{cl} is given by

$$D_{cl} = Cm_{cl}^{\gamma} \tag{3.8}$$

where C is a constant and γ accounts for effects from cluster geometry [12]. In the case of a cluster in a fluid, one expects that $\gamma \simeq -1/D_f$, since the mobility of a cluster in a fluid is inversely proportional to its hydrodynamic radius, which for an aggregate of fractal dimension D_f is close to its linear extension.

3.4 Distribution of particle diameter

In previous work by Häbel *et al.* (2019), the particle diameter was kept constant at 20 nm in the simulations, whereas in Köllerström (2020), the particles sizes were generated from different distributions that had been fitted to the nearest neighbor distances in the experimental data [1], [2]. This approach was used in this work as well; however, in Häbel et al. (2019) and Köllerström (2020), particles were generated until a volume fraction of 5.96 % was reached. A 5.96 % volume fraction corresponds to a weight percentage of 9 wt%, which was used in the experimental gel. In this study, the number of particles was instead set to be the same as the number of particles per volume unit in the experimental data. The distribution of particle sizes was estimated from the nearest neighbour distances $d_1, \ldots, d_n$ for the n particles by using kernel density estimation (KDE)

$$\hat{f}_h(d) = \frac{1}{nh} \sum_{i=1}^{n} K(\frac{d - d_i}{h}) \tag{3.9}$$

where $K(\cdot)$ is the kernel smoothing function and h is the bandwidth. The smoothing function $K(\cdot)$ was chosen as the standard normal density function, and the bandwidth was selected using Silverman's rule of thumb

$$h = 0.9 \min(\hat{\sigma}, \frac{\text{IQR}}{1.34}) n^{-\frac{1}{5}} \tag{3.10}$$

where $\hat{\sigma}$ is the sample standard deviation and IQR is the inter-quartile range of the data [13]. A proper choice of the bandwidth h is essential in order to avoid over-and under-smoothing. A histogram of the experimental data can be seen along with the estimated density in figure 3.1.

3.5 Models for sticking probability

In previous work done by Häbel *et al.* (2019) and Köllerström (2021) the sticking probability, i.e., the probability for particles to aggregate upon contact with each

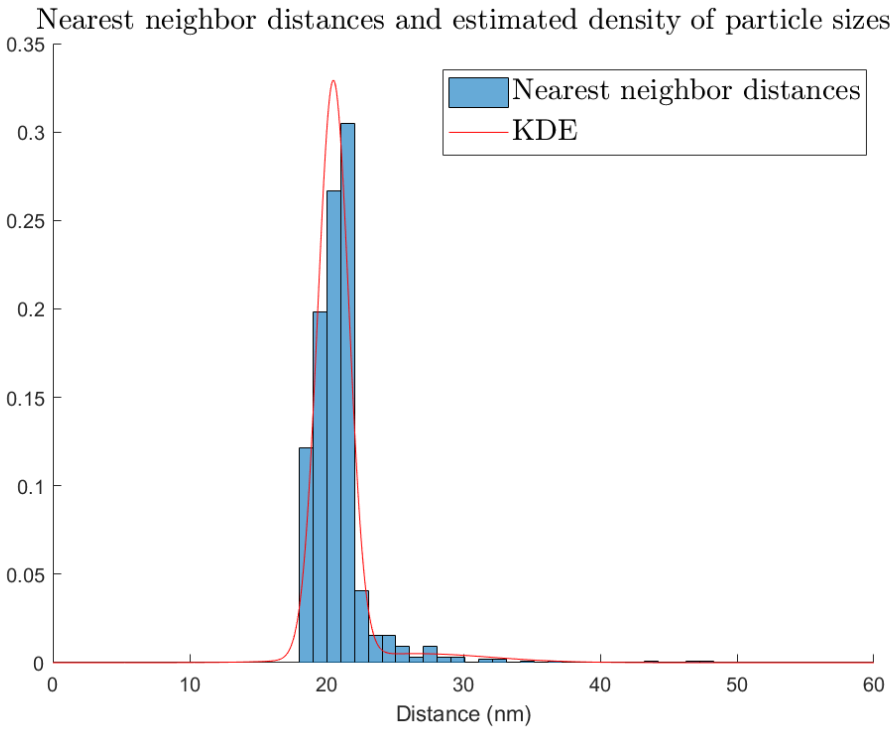


Figure 3.1: Histogram of nearest neighbor distances from the experimental data and the estimated probability density function of particle diameters.

other was assumed to be constant. Simulations with a constant sticking probability were carried out as part of this project as well, but in addition to this, two other functions for the sticking probability were tested. The functions for the sticking probabilities presented in sections 3.5.1, 3.5.2 and 3.5.3 will be referred to as models 1, 2 and 3, respectively.

3.5.1 Constant sticking probability

Since the concentration and sizes of particles had been estimated differently compared to previous studies, it was seen as interesting to carry out simulations with a constant sticking probability. The values that were investigated in the studies by Häbel *et al.* (2019) and Köllerström (2021) were

$$p \in \{1, 0.1, 0.01, 0.001, 0.0001\}. \tag{3.11}$$

In Häbel *et al.* (2019) the best fit overall was obtained with $p = 0.0001$ whereas in Köllerström (2020) the overall best value was concluded to be $p = 0.01$. The set of values in equation 3.11 were used in this thesis as well in order to make comparisons to the previous studies.

3.5.2 Sticking probability dependent on cluster size

In the second model that was tested, the sticking probability was made dependent of the masses of the two colliding clusters. Several previous cluster aggregation studies,

including studies of silica specifically, have studied cluster aggregation simulations carried out with a sticking probability of the form

$$p(S_1, S_2) = \min(1, p_0(S_1 \cdot S_2)^\sigma) \tag{3.12}$$

where S_1 and S_2 are the number of particles in the two colliding aggregates while $p_0 \in [0, 1]$ and $\sigma \in \mathbb{R}$ are model parameters [14], [15], [16]. Thus, collisions between single particles have the probability p_0, and σ decides how this probability changes with the cluster size. In order to take into account that particles in our simulation have different sizes and that the mass of an aggregate is not proportional to the number of particles in it, the sticking probability was instead expressed in terms of the masses m_1 and m_2 of the two colliding clusters through

$$p(m_1, m_2) = \min\left(1, p_0\left(\frac{m_1}{\overline{m}}\right)^\sigma\left(\frac{m_2}{\overline{m}}\right)^\sigma\right). \tag{3.13}$$

where $\overline{m}$ is the average mass of a particle in the simulation. The parameter values used in this study can be found in table 3.1.

$p_0 = 1$	$\sigma = -0.5, -0.25$
$p_0 = 0.1$	$\sigma = -0.5, -0.25, 0.25, 0.5$
$p_0 = 0.01$	$\sigma = -0.25, 0.25, 0.5$
$p_0 = 0.001$	$\sigma = 0.25, 0.5$
$p_0 = 0.0001$	$\sigma = 0.25, 0.5$

Table 3.1: Every row contains the values of p_0 and σ that have been tried in combination when simulating with model 2.

3.5.3 Sticking probability dependent on particles close to collision

The third model tested was a sticking probability dependent on the number of particles close to the collision. More specifically, let C_1 and C_2 denote two colliding clusters and let d_{ij} be the distance between the *surfaces* of two particles i and j. Then the sticking probability for a collision between particles $i \in C_1$ and $j \in C_2$ can be written as

$$p = \min\left(1, p_0 + \delta\left(\sum_{k:k\in C_1, k\neq i} \mathbb{1}(d_{kj} \leq s) + \sum_{k:k\in C_2, k\neq j} \mathbb{1}(d_{ik} \leq s)\right)\right) \tag{3.14}$$

where $p_0 \in [0, 1]$ and $\delta, s \geq 0$ are the parameters of the model. Hence, the probability of a collision is p_0 and then increases with δ for every other particle in an opposite cluster that has surface within distance s from the colliding ones (see figure 3.2). It can be seen as taking into account multiple particle interactions at the collision site. The values that were tested in this work were all combinations of

$$\begin{aligned} p_0 &\in \{0.01, 0.001, 0.0001\} \\ \delta &\in \{0.01, 0.001, 0.0001\} \\ s &\in \{0.5, 2.5, 4.5, 6.5\} \end{aligned}$$

with s given in nm.

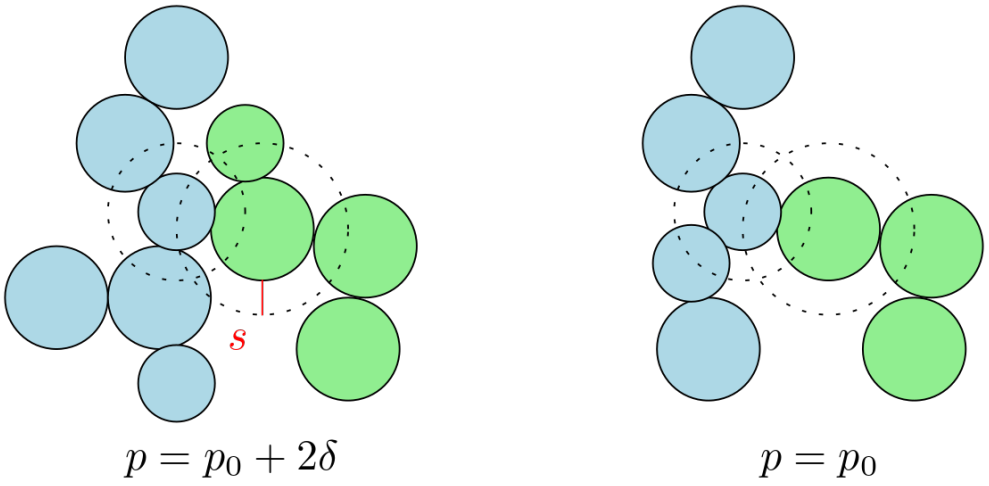


Figure 3.2: Illustration of how the sticking probability in equation 3.14 is calculated.

3.6 Implementation

The aggregation simulations were carried out using Fortran code, written by Matias Nordin and Tobias Gebäck, which was called from Matlab. The main modifications to this code were to allow particles to have different sizes and use different functions for the sticking probability. No rearrangement of particles due to bond breakage or rotational rearrangement was included. Gravitational effects and rotational diffusion were also disregarded in this study. The computations were enabled by resources provided by the Swedish National Infrastructure for Computing (SNIC) at Chalmers Centre for Computational Science and Engineering (C3SE), partially funded by the Swedish Research Council through grant agreement no. 2018-05973.

4

Model Evaluation

This chapter describes the methods used for comparing the simulated structures to the experimental data. The main part of the model evaluation consists of comparing the spatial structure through spatial summary statistics from point process theory. Parameters are selected based on the goodness-of-fit of the spatial summary statistics, and further testing is then done by comparing fractal scaling and mass transport properties.

4.1 Spatial Point Processes

This part of the model evaluation focuses on the centroids of the particles, which form a point pattern. By regarding such a point pattern as a realization of a point process, one can use summary statistics from point process theory to characterize the point pattern.

4.1.1 Basic Definitions

In this section, we start by giving a formal definition of point processes along with their distributions which mainly follow the book *Stochastic Geometry and its Applications* by Stoyan *et al.* (2013) [17]. The characteristics *stationarity* and *isotropy* are defined as well as the *intensity*. Throughout section 4.1, we let $\mathcal{B}(\mathbb{R}^d)$ denote the Borel sets on $\mathbb{R}^d$ and $\mathcal{B}_0(\mathbb{R}^d)$ the family of all bounded Borel sets on $\mathbb{R}^d$. The $d-$dimensional Lebesgue measure is denoted as $\nu_d(\cdot)$ while $\partial(A)$ is the boundary of a set $A \subset \mathbb{R}^d$.

4.1.1.1 Point Process

In order to define a point process on $\mathbb{R}^d$ for $d \geq 1$ we first consider a probability space $(\Omega, \mathcal{F}, \mathbf{P})$ and a measurable space $(\mathbb{N}, \mathcal{N})$. Here $\mathbb{N}$ is the family of sequences $\varphi = \{x_n\}$ of points of $\mathbb{R}^d$ that satisfy two conditions:

- The sequence φ is *locally finite*, meaning that every $B \in \mathcal{B}(\mathbb{R}^d)$ must only contain a finite number of points of φ.

- The sequence φ is *simple*, meaning that two points in the sequence, x_i and x_j, cannot be equal if $i \neq j$.

The σ-algebra $\mathcal{N}$ is defined as the smallest σ-algebra on $\mathbb{N}$ that makes all mappings $\varphi \mapsto \varphi(B)$ measurable, for $B \in \mathcal{B}_0(\mathbb{R}^d)$ and where $\varphi(B)$ denotes the number of points in the set B.

A formal definition of point process Φ is that it is a measurable mapping of a probability space $(\Omega, \mathcal{F}, \mathbb{P})$ into $(\mathbb{N}, \mathcal{N})$ as above. More intuitively, it can be thought of as a random choice of one of the φ in $\mathbb{N}$. As such, it generates a distribution P on $[\mathbb{N}, \mathcal{N}]$, which is called the distribution of the point process Φ.

4.1.1.2 Notation

Point processes can be interpreted in two different ways, either as random sets of discrete points or as random measures that count how many points that lie in certain spatial regions. Two different notations correspond to these interpretations:

- $x \in \Phi$, denoting that the point x belongs to the random sequence Φ
- $\Phi(B) = n$, denoting that the set B contains n points of Φ.

In this section, we will switch between these interpretations depending on what best suits the context.

4.1.1.3 Distributions

The distribution P of a point process is determined as

$$P(Y) = \mathbb{P}(\Phi \in Y) = \mathbb{P}(\{\omega \in \Omega : \Phi(\omega) \in Y\}), \text{ for } Y \in \mathcal{N}. \tag{4.1}$$

Here the meaning of $\Phi \in Y$ is that it specifies that Φ has property Y, and $\mathbb{P}(\Phi \in Y)$ denotes the probability that Φ has this property. We might, for instance, be interested in looking at the probability that the point process contains a certain number of points in different sets

$$\mathbb{P}(\Phi(B_1) = n_1, \ldots, \Phi(B_k) = n_k) \tag{4.2}$$

where $B_1, B_2, \ldots, B_k \in \mathcal{B}(\mathbb{R}^d)$ and $n_1, \ldots, n_k \geq 0$. The expression in equation 4.2 denotes the probability that the point process Φ has n_1 points in B_1, n_2 points in B_2, ... and n_k points in B_k. These probabilities are sometimes called the *finite-dimensional distributions*.

A special case of the above probabilities is the *void-probabilities*

$$P(\{\varphi \in \mathbb{N} : \varphi(B) = 0\}) = \mathbb{P}(\Phi(B) = 0), \quad \text{for } B \in \mathcal{B}(\mathbb{R}^d). \tag{4.3}$$

The interpretation is that equation 4.3 gives us the probability that B does not contain any points of Φ.

4.1.1.4 Stationarity and Isotropy

A point process is said to be *stationary* if its distribution is invariant under translation. Let $\Phi = \{x_1, \ldots, x_n\}$ and $\Phi_x = \{x_1 + x, \ldots, x_n + x\}$ with $x \in \mathbb{R}^d$. Then for a stationary point process, we have that

$$\mathbb{P}(\Phi \in Y) = \mathbb{P}(\Phi_x \in Y) \tag{4.4}$$

for all configuration sets Y.

The concept of *isotropy* is analogous to that of stationarity, but instead means that the distribution of the point process is invariant under rotation around the origin. If we let R be a rotation matrix, then a point process Φ is isotropic if

$$\mathbb{P}(\Phi \in Y) = \mathbb{P}(R\Phi \in Y.) \tag{4.5}$$

4.1.1.5 Intensity measure and intensity

The intensity measure $\Lambda : \mathcal{B}(\mathbb{R}^d) \to [0, \infty)$ of a point process Φ is similar to the expected value of a random variable. It is given by

$$\Lambda(B) = \mathbb{E}[\Phi(B)] = \int_B \lambda(s)ds, \quad \text{for } B \in \mathcal{B}(\mathbb{R}^d), \tag{4.6}$$

in the case when Λ has an intensity λ: $\mathcal{B}(\mathbb{R}^d) \to [0, \infty)$ with respect to the Lebesgue measure. [18]. Hence, $\Lambda(B)$ is the mean number of points in B.

If the point process is stationary, then the intensity measure must also be translation invariant since

$$\Lambda(B) = \mathbb{E}[\Phi(B)] = \mathbb{E}[\Phi_x(B)] = \mathbb{E}[\Phi(B_{-x})] = \Lambda(B_{-x}), \quad \text{for all } x \in \mathbb{R}^d. \tag{4.7}$$

It then follows that the intensity measure can be written in the form

$$\Lambda(B) = \lambda v_d(B), \tag{4.8}$$

where λ is a non-negative constant. If we take B of volume 1, we see that λ can be interpreted as the mean number of points per volume unit. For the rest of this section we assume that $0 < \lambda < \infty$.

4.1.2 Summary Statistics

In this section, we introduce four summary statistics that are used to compare the simulated structures and the ones in the experimental data by considering the centroids of the particles as point patterns. The summary statistics are the *empty space function*, *L-function*, *clustering function* and the *mean cluster size function*. All these summary statistics can be estimated from the observations of a point process Φ inside an observational window W in $\mathbb{R}^d$. We assume that the observed point process Φ is stationary and isotropic. For the rest of this section, we will let $d = 3$, since we work with data and simulations in 3D.

4.1.2.1 Empty Space Function

The empty space function $F : [0, \infty) \to [0, 1]$ gives the probability that the distance from an arbitrary test point $o \in \mathbb{R}^3$ to its nearest neighbor in Φ is less than or equal to $r \geq 0$ [19]. It is a valuable summary statistic to describe the amount of empty space between clusters of points but is less useful for describing the actual clusters. Start by denoting the shortest euclidean distance between o and any closed set $A \in \mathbb{R}^3$ as

$$p(o, A) = \inf(||o - a||_2 : a \in A). \tag{4.9}$$

Let $b(o, r)$ be the ball of radius $r \geq 0$ centered at $o \in \mathbb{R}^3$. The *empty space function* is then given as

$$F(r) = \mathbb{P}(p(o, \Phi) \leq r) = 1 - \mathbb{P}(\Phi(b(o, r)) = 0). \tag{4.10}$$

An unbiased estimator for the empty space function is given by a Kaplan-Meier estimator with hazard rate

$$\hat{h}(r) = \frac{\nu_2(\partial(\Phi_{\oplus r}) \cap W_{\ominus r})}{\nu_3(W_{\ominus r} \backslash \Phi_{\oplus r})}. \tag{4.11}$$

for $\Phi_{\oplus r} = \Phi \oplus b(o, r)$ where $\oplus$ is the Minkowski addition and $W_{\ominus r} = W \ominus b(o, r)$ where $\ominus$ is Minkowski subtraction. We can note that the sets

$$\{o \in W : \min(p(o, \Phi), p(o, \partial W)) \geq r\}$$
$$\text{and } \{o \in W : p(o, \Phi) = r, p(o, \Phi) \leq p(o, \partial W)\}$$

are the closures of $W_{\ominus r} \backslash \Phi_{\oplus r}$ and $\partial(\Phi_{\oplus r}) \cap W_{\ominus r}$ respectively. These sets may be interpreted in our context as the points "at risk of failure at distance r" and "observed failures at distance r", where a failure would be for a point o to have $p(o, \Phi) = r$. The full estimator for $F(r)$ is then given by

$$\hat{F}(r) = 1 - \exp\left[-\int_0^r \hat{h}(s)ds\right]. \tag{4.12}$$

for $r \geq 0$.

4.1.2.2 L-function

A commonly used second-order characteristic is *Ripley's K-function* $K : [0, \infty) \to [0, \infty)$, which measures the average number of points that can be found within a distance $r \geq 0$ from an arbitrary point o of the process Φ [1]. If λ denotes the intensity, the K-function is defined as

$$K(r) = \lambda^{-1}\mathbb{E}_o[\Phi(b(o, r)) \backslash o] \tag{4.13}$$

for $r \geq 0$ and where $\mathbb{E}_o$ is the expectation given that there is a point of Φ in o.

In order to estimate the K-function, one might consider using an estimator of the form

$$\frac{\nu_3(W)}{n(n-1)} \sum_{i=1}^{n} \sum_{j \neq i} \mathbb{1}(d_{ij} \leq r). \tag{4.14}$$

where $n = \Phi(W)$ and d_{ij} is the pairwise inter-point distances between points in $\Phi \cap W$. However, this estimator is biased, and we need to account for the edges of the observational window W. To correct this, Ripley's isotropic edge correction can be used, in which every term in equation 4.14 is adjusted by the fraction of the search ratio that lies within the observational window W. This is done through the weights w_{ij} so that

$$\hat{K}(r) = \frac{\nu_3(W)}{n(n-1)} \sum_{i=1}^{n} \sum_{j \neq i} w_{ij}^{-1} \mathbb{1}(d_{ij} \leq r). \tag{4.15}$$

where

$$w_{ij} = w(x_i, d_{ij}) = \frac{\nu_2(\partial(x_i, d_{ij}) \cap W)}{\nu_2((x_i, d_{ij}))}. \tag{4.16}$$

The K-function is often not studied directly. Instead, it is common to use summary statistics based on the K-function with stabilized variance. In this project we use the L-function $L : [0, \infty) \to [0, \infty)$ which is given as

$$L(r) = \sqrt[3]{\frac{3K(r)}{4\pi}}, \quad \text{for } r \geq 0. \tag{4.17}$$

We get an estimator $\hat{L}$ for this summary statistic by simply using $\hat{K}(r)$ instead of $K(r)$ in the expression above.

4.1.2.3 Clustering function

The clustering function $c : [0, \infty) \to [0, 1]$ is a third order characteristic based on graph theory which was extended to point processes by Rajala (2010) [20]. In the clustering function, one considers triplets of points within some distance r and compares it to the maximal theoretical number of triplets. As such, the summary statistic can be interpreted as a measure of the internal connectivity around an arbitrary point at distance r. For $o \in \Phi$ the number of triplets within a distance r from o is given by

$$\Delta_{o,r} = \sum_{i,j : x_i, x_j \in \Phi \cap b(o,r) \setminus \{o\}} \mathbb{1}(d_{ij} \leq r). \tag{4.18}$$

The theoretical number of possible triplets for $o \in \Phi$ within a distance r is obtained as

$$\Delta_{o,r}^{\max} = \binom{\delta(o)}{2} = \frac{1}{2}(\delta(o)^2 - \delta(o)), \quad \text{where} \quad \delta(o) = \sum_{i : x_i \in \Phi \setminus \{o\}} \mathbb{1}(||o - x_i|| \leq r). \tag{4.19}$$

In order to compare the observed and theoretical number of triplets, we consider

$$C_{o,r} = \begin{cases} \Delta_{o,r} / \Delta_{o,r}^{\max}, & \text{if } \delta(o) \geq 2 \\ 0, & \text{if } \delta(o) < 2 \end{cases} \tag{4.20}$$

and then take the expected value $c(r) = \mathbb{E}[C_{o,r} | o \in \Phi] = \mathbb{E}_o[C_{o,r}]$.

We can estimate $c(r)$ as $\tilde{c}(r) = \mathbb{E}_o[\Delta_{o,r}]/\mathbb{E}_o[\Delta_{o,r}^{\max}]$ by using that

$$\mathbb{E}_o[\Delta_{o,r}] \approx \frac{1}{n} \sum_{i:x_i \in \Phi \cap W} \sum_{\substack{j,k:x_j,x_k \in \\ \Phi \cap W \cap b(x_i,r) \setminus \{x_i\}}} \mathbb{1}(||x_j - x_k|| < r) \tag{4.21}$$

and

$$\mathbb{E}_o[\Delta_{o,r}^{\max}] \approx \frac{1}{n} \sum_{i:x_i \in \Phi \cap W} \frac{1}{2}(\delta(x_i)^2 - \delta(x_i)), \tag{4.22}$$

where $n = \Phi(W)$. Edge effects can be handled by applying the *minus-sampling* scheme where we only use points within the eroded window $W_{\ominus,r}$ (see figure 4.1).

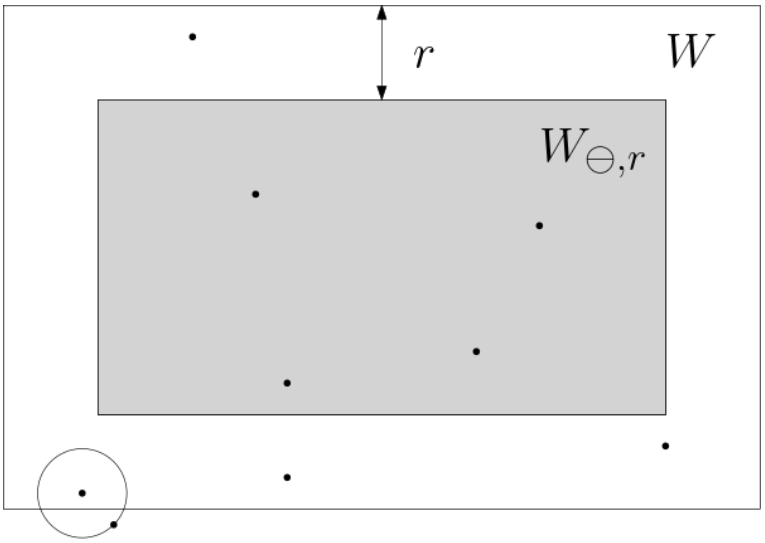


Figure 4.1: The observational window W and the eroded window $W_{\ominus,r}$, which is shaded in grey. We can see that for points in $W \backslash W_{\ominus,r}$ there is the possibility that points have neighbors at distances smaller than r that we do not observe.

4.1.2.4 Mean cluster size function

The mean cluster size function $M : [\infty, 0) \to [\infty, 0)$ is a summary statistic that describes how dense and spread out the clusters are [1]. From the points x in $\Phi \cap W$ we create a geometric graph with nodes in the points x and connect all points x_i and x_j for which $d_{ij} \leq r$. A cluster at distance r can then be defined as the set of all points that are connected by such edges. Assume that there are K clusters for distance r and that cluster k has n_k points in it. The size of cluster k can then be measured by using the diameter of gyration

$$D_k(r) = \frac{1}{n_k} \sqrt{2 \sum_{i=1}^{n_k} \sum_{j=1}^{n_k} d_{ij}^2}. \tag{4.23}$$

The mean cluster size function in three dimensions for distance r was defined by Häbel *et al.* (2019) as

$$M(r) = \frac{1}{K} \sum_{k=1}^{K} D_k(r), \tag{4.24}$$

for $r \geq 0$. In order to account for edge effects, we can use the minus-sampling scheme.

4.1.3 Evaluation of models based on functional summary statistics

In the following sections, the evaluation of the goodness-of-fit of the spatial summary statistics is explained, and how the best model and parameters were selected. For the best model, global envelope tests were conducted to compare the model with the experimental data further.

4.1.3.1 Parameter selection

The best sets of parameters for every model were selected based on the four summary statistics introduced in section 4.3.2 by performing simulations in a $700 \times 700 \times 700$ nm^3 box with periodic boundary conditions. The summary statistics were calculated for r in the range 0-50 nm. To achieve more robust results, the experimental and simulated data were divided into subpatterns for which the summary statistics were calculated and then averaged over. The real data was divided into 4 subpatterns of size $360 \times 520 \times 100$ nm^3 whereas the simulated data was divided into 6 subpatterns of the same size. These subpatterns had enough space between them to be considered independent replicates. The average over subpatterns was calculated by pooling according to

$$\hat{f}(r) = \frac{\sum_{i=1}^{n_{\text{pat}}} n_i f_i(r)}{\sum_{i=1}^{n_{\text{pat}}} n_i} \tag{4.25}$$

where n_{pat} is the number of subpatterns, $f_i(r)$ is the summary statistic for subpattern i at distance r and n_i is the number of points in subpattern i.

The pooled summary statistics from the simulated and STEM data were compared by using a least square approach similar to Redenbach and Särkkä (2013) [21]. By calculating the pooled summary functions at equally spaced distances $r_1, \ldots, r_T$, the sum of squares could be obtained as

$$S_j = \frac{1}{T} \sum_{t=1}^{T} \left(\frac{\tilde{\hat{f}}_j(r_t) - \hat{f}_j(r_t)}{\hat{f}_j(r_t)} \right)^2 \tag{4.26}$$

where j goes through the different summary statistics F, L, c, M and $\hat{f}_j(\cdot)$ and $\tilde{\hat{f}}_j(\cdot)$ is the pooled summary statistic from the experimental and simulated data respectively. The total sum of squares of the evaluated summary statistics is then given as

$$S = S_F + S_L + S_c + S_M, \tag{4.27}$$

and was calculated for all simulations to select the best parameters for every model of the sticking probability.

4.1.3.2 Global envelope test

After selecting a candidate model based on the total sum of squares in equation 4.27, a *global envelope test* was conducted to make a more detailed comparison between the selected model and the experimental data. In a global envelope test, one tests if a certain null model is appropriate to describe an observed point pattern based on performing Monte Carlo simulations from the chosen model and then comparing summary statistics from the simulated and observed patterns. More explicitly, let $T_{\text{obs}}(r)$ be the value of a summary statistic estimated from the observed data at distance $r \geq 0$. An *envelope* is a band bounded by the functions $T_{\text{low}}(r)$ and $T_{\text{upp}}(r)$ on an interval I [22]. A global envelope test is a statistical test that rejects the null hypothesis H_0, i.e., that the null model is appropriate for the data, in the case that the observed function $T_{\text{obs}}(r)$ is not completely inside the envelope

$$\varphi_{\text{env}}(T_{\text{obs}}) = \mathbb{1}(\exists r \in I : T_{\text{obs}}(r) \notin (T_{\text{low}}(r), T_{\text{upp}}(r))). \tag{4.28}$$

It is desirable to establish the bounds so that the test has a controlled global type I probability for a certain number of simulations n_{sim}.

In this study, a type of global scaled maximum absolute difference (MAD) envelope test was chosen for which the recommended number of simulations n_{sim} was small, typically $n_{\text{sim}} = 99$ or $n_{\text{sim}} = 199$ [23], [24]. More specifically, the *directional quantile* MAD envelope test was used in which the critical bounds are given by

$$T^u_{\text{low}}(r) = T_0(r) - u \cdot |\underline{T}(r) - T_0(r)| \quad \text{and} \quad T^u_{\text{low}}(r) = T_0(r) + u \cdot |\overline{T}(r) - T_0(r)|. \tag{4.29}$$

Here, $T_0(r)$ is the expectation under the null model and $\overline{T}(r)$ and $\underline{T}(r)$ are the r-wise 2.5% upper and lower quantiles of the distribution of $T(r)$ under H_0. Since neither of these are known analytically, they were estimated from the simulations of the null model. For the directional quantile MAD envelope test, u is taken as

$$u = \max_{r \in I} \left(\mathbb{1}(T(r) \geq T_0(r)) \frac{T(r) - T_0(r)}{|\overline{T}(r) - T_0(r)|} + \mathbb{1}(T(r) < T_0(r)) \frac{T(r) - T_0(r)}{\underline{T}(r) - T_0(r)} \right). \tag{4.30}$$

and a $100(1-\alpha)\%$ envelope from s simulations is obtained by using the $\alpha(s+1)$th largest value of the u's in equation 4.30 for the bounds in equation 4.29. In addition to only requiring a small number of simulations, this test considers variations of the variance for the summary statistic for different values of r as well as asymmetry in the distribution, which both seemed to be features of the simulated summary statistics when inspecting the data.

4.1.4 Computational tools

The spatial data analysis was conducted in the R software version 4.1.3 with the packages **spatstat**, **GET**, and a slightly modified version of the **SGCS** package. Code written by Henrike Häbel that had been used in previous studies was received at the start of this project.

4.2 Fractal scaling properties

In section 3.3 it was mentioned that structures from DLCA and RLCA simulations have been found to have fractal scaling properties. The fractal dimension has also been used to compare the experimental STEM data and the simulated structures. The fractal dimensions of the experimental and simulated structures were calculated using a version of the box-counting algorithm. In the box-counting algorithm, one chooses a box that covers the structure, referred to as the bounding box, and places evenly spaced grids with boxes with side length ϵ within the bounding box. The minimal number of boxes $N(\epsilon)$ needed to cover the set is calculated, and the fractal dimension can be estimated from how $N(\epsilon)$ scales with the box size. For a set S in $\mathbb{R}^n$, the box-counting dimension is defined as

$$D_{\text{box}}(S) = -\lim_{\epsilon \to 0} \frac{\log(N(\epsilon))}{\log(\epsilon)}. \tag{4.31}$$

Roughly speaking, a set with a non-integer box-counting dimension is considered to have fractal geometry since it suggests that it scales differently from the space that it resides in [25].

In practical settings, the limit in equation 4.31 cannot be taken, and the box-counting dimension is instead estimated through the slope between $\log(N(\epsilon))$ and $\log(\epsilon)$ as ϵ decreases. The idea of the box-counting algorithm is to choose a set of decreasing box sizes $\epsilon_1, \ldots, \epsilon_n$ and calculate the corresponding $N(\epsilon_1), \ldots, N(\epsilon_n)$ from which the box-counting dimension can be approximated by performing linear regression. The total volume of the analysis should be kept the same for all box sizes.

The choice of the box sizes $\epsilon_1, \ldots, \epsilon_n$ can heavily influence the estimated fractal dimension [26]. A slight modification of the standard box-counting algorithm was used in which the positions of the boxes were uniformly generated inside the bounding box. Then the number of non-empty boxes was normalized with the total volume of the generated boxes. As a consequence, the box sizes do not have to be chosen in such a way that the bounding box can be decomposed into an integer number of boxes to keep the total volume of analysis constant for different box sizes (see figure 4.2) [26]. Furthermore, effects from the overall placement of boxes is reduced using this method.

4.3 Mass transport

The simulated materials and the data were compared also based on simulating mass transport through the materials. Simulations of both flow and diffusion were carried out as part of this study.

4.3.1 Flow

When a fluid is transported along, for example, a pressure or gravitational gradient, we call it a flow [4]. In the case of a steady and laminar flow and the pores in the

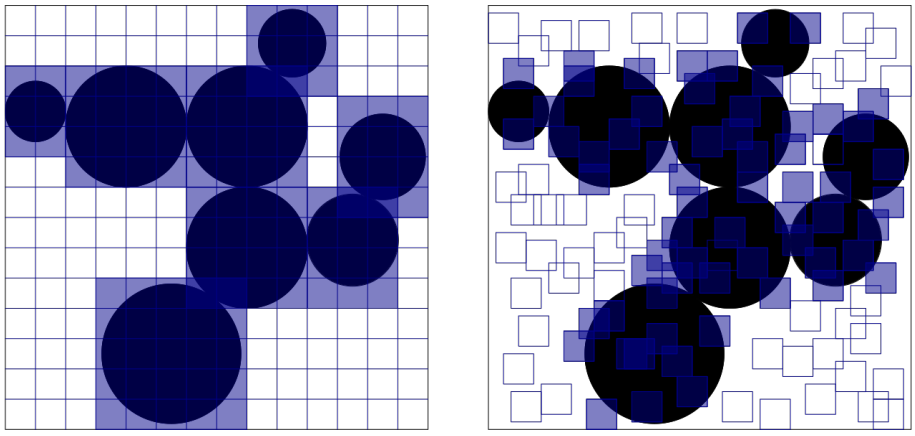


Figure 4.2: Illustration of the normal box counting procedure to the left and the random box counting on the right.

gel can be regarded as straight pipes, we can use the Hagen-Poiseuille relationship

$$Q = \frac{\pi R^4}{8L\eta}\Delta p \tag{4.32}$$

to determine how the volumetric flow rate Q (with units of m^3/s) is transported through a pipe with radius R and length L. η denotes the dynamic viscosity of the fluid, and Δp is the pressure difference that drives the flow. From equation 4.32 we see that the flow through the pipe is proportional to R^4, meaning that the radius greatly impacts the flow through the material. Therefore, parts of the structure with much empty space can greatly impact the overall flow through the material.

Another characteristic of the material that tells us how easily flow can pass through it is the permeability κ defined through Darcey's law

$$q = \frac{-\kappa}{\eta L}\Delta p \tag{4.33}$$

where q is the average flow velocity ($q = Q/A$ where A is the cross-sectional area) [27]. Unlike the Hagan-Poiseuille relationship, which describes flow through a circular pipe, Darcey's law is valid for any porous material assuming steady laminar flow.

In order to characterize the flow as laminar or turbulent, one can use the *Reynold's number* (Re), which is a dimensionless ratio between inertial and frictional forces in the flow

$$\mathrm{Re} = \frac{F_{\text{inertial}}}{F_{\text{viscous}}} = \rho\frac{vl}{\eta}. \tag{4.34}$$

Here v and l denotes the investigated system's characteristic velocities and length scales, and ρ is the density of the fluid. Typically, any flow with Reynold's number less than unity can be considered clearly laminar, and it would be valid to apply Darcey's law [27]. In this project, the characteristic length scale is very small, and the relevant flows are highly laminar.

4.3.2 Diffusion

Diffusion was presented in section 2.1.1 in the context of aggregation of silica particles. In this section, we instead consider the diffusion of molecules through a porous material along a concentration gradient. As before, the individual movement of particles is governed by Brownian motion, but differences in concentration will eventually fade away. In the diffusion simulations, the diffusion equation from before is solved

$$\frac{\partial \varphi(x,t)}{\partial t} = D_0 \nabla^2 \varphi(x,t) \tag{4.35}$$

with the free diffusion coefficient D_0. The effective diffusion coefficient D_{eff} will then be computed from Fick's first law

$$\overline{j} = -D_{\text{eff}} \frac{\varphi_2 - \varphi_1}{d} \tag{4.36}$$

where $\overline{j}$ is the average flux, $\varphi_2 - \varphi_1$ is the concentration difference over the material, and d is the thickness of the material. The effective diffusion coefficient D_{eff} is proportional to the free diffusion coefficient D_0, and in order to get a quantity that only depends on the geometry of the aggregate, we can calculate

$$G = \frac{D_{\text{eff}}}{D_0} \tag{4.37}$$

which will be called the geometry factor [28].

4.3.3 Software

Flow and diffusion simulations were performed using the lattice Boltzmann method-based software Gesualdo, developed as a part of the SuMo Biomaterials collaboration at Chalmers [29].

5
Results

5.1 Goodness of fit for summary statistics

The results from comparing the spatial summary statistics from simulated and experimental data are presented in the following sections.

5.1.1 Constant sticking probability

The values for the total sum of squares S in equation 4.27 for different parameters with model 1 can be seen in figure 5.1 and table 5.1. The sum of squares decreases significantly between $p = 0.1$, $p = 0.01$ $p = 0.001$, while there is a smaller difference between $p = 0.001$ and $p = 0.0001$. The smallest value of S was obtained for $p = 0.0001$ and resulted in $S \approx 0.0819$. Plots of the summary statistics can be found in figure 5.2. At distances larger than 25-30 nm, all the summary statistics seem to deviate systematically from the experimental data. The empty space function suggests that there is more empty space in the experimental data for large values of r. Looking at the L-function, it is evident that the simulated data appears to be less clustered than the STEM data. For the c-function, the simulated structure is initially less clustered, but as r gets larger the function increases and passes the experimental data. The M-function fits the STEM data up until approximately $r = 28$ nm and then results in smaller values.

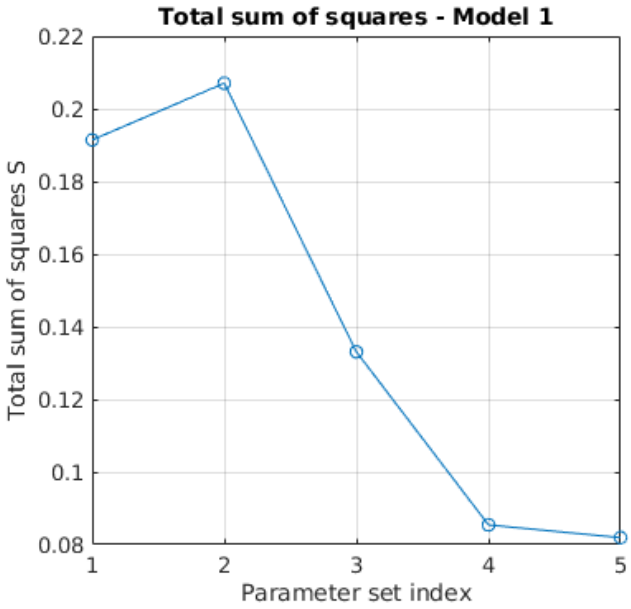


Figure 5.1: Total sum of squares from simulations with model 1.

Index	Parameters
1	$p = 1$
2	$p = 0.1$
3	$p = 0.01$
4	$p = 0.001$
5	$p = 0.0001$

Table 5.1: Parameters that correspond to the different indices in figure 5.1

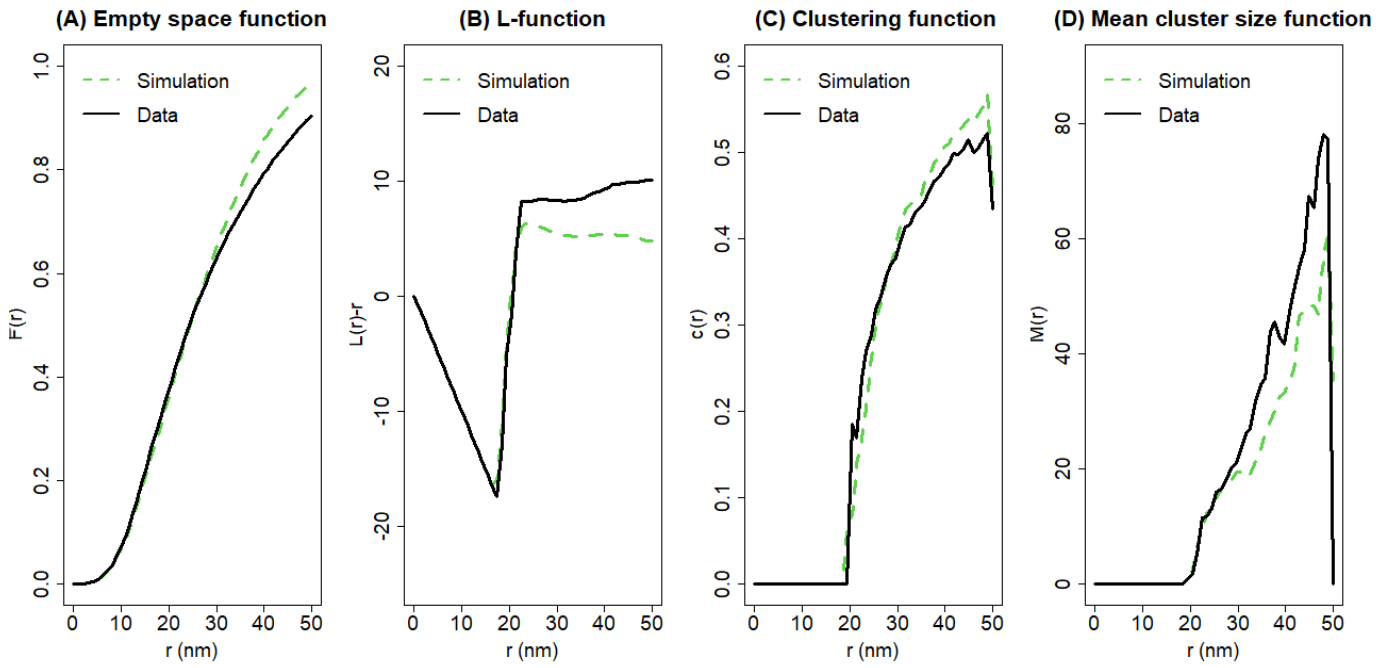


Figure 5.2: Pooled averages for the four summary statistics from simulation with a constant sticking probability $p = 0.0001$ (green) and from the STEM-data (black).

5.1.2 Mass dependent sticking probability

Results from all simulations with model 2 can be seen in figure 5.3 and table 5.2. All simulations with $\sigma < 0$ improve the sum of squares compared to model 1 with the same value of p_0. However, there is also one simulation with a positive σ that improves the goodness-of-fit. The lowest value of S was obtained with $p_0 = 0.01$ and $\sigma = -0.25$ resulting in $S \approx 0.0657$. This corresponds to a decrease of approximately 19.8% of S compared to the best simulation using model 1. The values of the summary statistics can be seen in figure 5.4. The main improvement compared to the best simulation from using a constant sticking probability is the fit of the mean cluster size function.

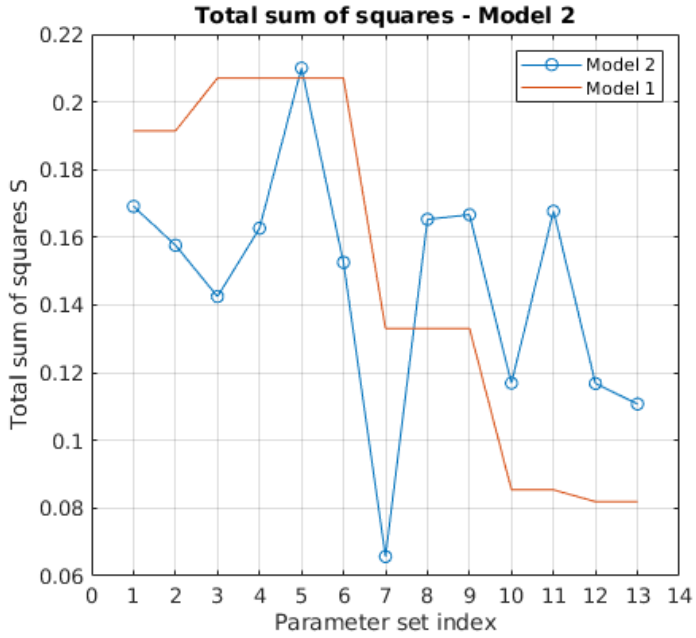


Figure 5.3: Total sum of squares S from simulations with model 2 (blue) and corresponding value of S from model 1 with $p = p_0$ (orange).

Index	Parameters
1	$p_0 = 1, \sigma = -0.5$
2	$p_0 = 1, \sigma = -0.25$
3	$p_0 = 0.1, \sigma = -0.5$
4	$p_0 = 0.1, \sigma = -0.25$
5	$p_0 = 0.1, \sigma = 0.25$
6	$p_0 = 0.1, \sigma = 0.5$
7	$p_0 = 0.01, \sigma = -0.25$
8	$p_0 = 0.01, \sigma = 0.25$
9	$p_0 = 0.01, \sigma = 0.5$
10	$p_0 = 0.001, \sigma = 0.25$
11	$p_0 = 0.001, \sigma = 0.5$
12	$p_0 = 0.0001, \sigma = 0.25$
13	$p_0 = 0.0001, \sigma = 0.5$

Table 5.2: Parameters that correspond to the different indices in figure 5.3

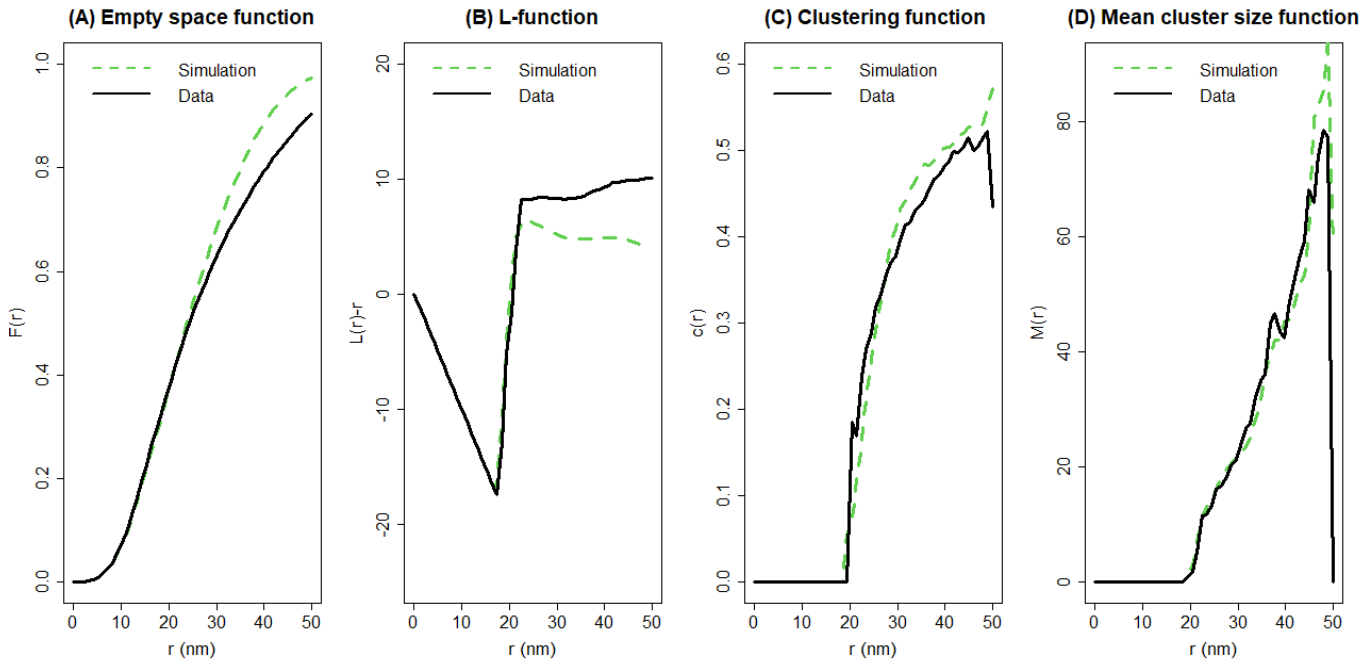


Figure 5.4: Pooled averages for the four summary statistics from simulation with a mass-dependent sticking probability with $p_0 = 0.01$ and $\sigma = -0.25$, and from the STEM-data (black).

5.1.3 Sticking probability dependent on the number of particles close to collision

Figure 5.5 and table 5.3 contains the results of S from the simulations with model 3. Simulation 32 gives a much larger value of S than the other simulations. From inspecting the summary statistics, it was seen that the mean cluster size function from simulation 32 is much greater than for the experimental data. The smallest value of S using model 2 was obtained with $p_0 = 0.0001$, $\delta = 0.001$ and $s = 2.5$ nm. This resulted in $S \approx 0.0534$, which is approximately 34.7% smaller than when using a constant sticking probability.

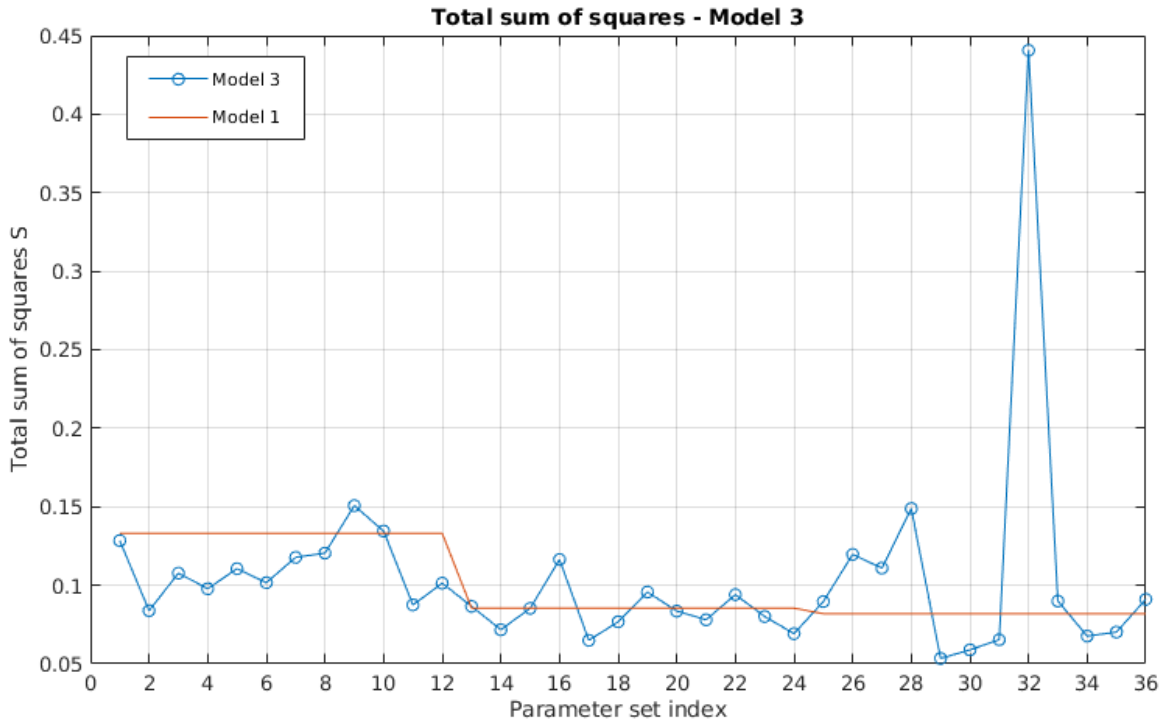


Figure 5.5: Total sum of squares S from simulations with model 2 (blue) and corresponding value of S from model 1 with $p = p_0$ (orange).

Index	Parameters	Index	Parameters	Index	Parameters
1	$p_0 = 0.01, \delta = 0.01, s = 0.5$	13	$p_0 = 0.001, \delta = 0.01, s = 0.5$	25	$p_0 = 0.0001, \delta = 0.01, s = 0.5$
2	$p_0 = 0.01, \delta = 0.001, s = 0.5$	14	$p_0 = 0.001, \delta = 0.001, s = 0.5$	26	$p_0 = 0.0001, \delta = 0.001, s = 0.5$
3	$p_0 = 0.01, \delta = 0.0001, s = 0.5$	15	$p_0 = 0.001, \delta = 0.0001, s = 0.5$	27	$p_0 = 0.0001, \delta = 0.0001, s = 0.5$
4	$p_0 = 0.01, \delta = 0.01, s = 2.5$	16	$p_0 = 0.001, \delta = 0.01, s = 2.5$	28	$p_0 = 0.0001, \delta = 0.01, s = 2.5$
5	$p_0 = 0.01, \delta = 0.001, s = 2.5$	17	$p_0 = 0.001, \delta = 0.001, s = 2.5$	29	$p_0 = 0.0001, \delta = 0.001, s = 2.5$
6	$p_0 = 0.01, \delta = 0.0001, s = 2.5$	18	$p_0 = 0.001, \delta = 0.0001, s = 2.5$	30	$p_0 = 0.0001, \delta = 0.0001, s = 2.5$
7	$p_0 = 0.01, \delta = 0.01, s = 4.5$	19	$p_0 = 0.001, \delta = 0.01, s = 4.5$	31	$p_0 = 0.0001, \delta = 0.01, s = 4.5$
8	$p_0 = 0.01, \delta = 0.001, s = 4.5$	20	$p_0 = 0.001, \delta = 0.001, s = 4.5$	32	$p_0 = 0.0001, \delta = 0.001, s = 4.5$
9	$p_0 = 0.01, \delta = 0.0001, s = 4.5$	21	$p_0 = 0.001, \delta = 0.0001, s = 4.5$	33	$p_0 = 0.0001, \delta = 0.0001, s = 4.5$
10	$p_0 = 0.01, \delta = 0.01, s = 6.5$	22	$p_0 = 0.001, \delta = 0.01, s = 6.5$	34	$p_0 = 0.0001, \delta = 0.01, s = 6.5$
11	$p_0 = 0.01, \delta = 0.001, s = 6.5$	23	$p_0 = 0.001, \delta = 0.001, s = 6.5$	35	$p_0 = 0.0001, \delta = 0.001, s = 6.5$
12	$p_0 = 0.01, \delta = 0.0001, s = 6.5$	24	$p_0 = 0.001, \delta = 0.0001, s = 6.5$	36	$p_0 = 0.0001, \delta = 0.0001, s = 6.5$

Table 5.3: Parameters that correspond to the different indices in figure 5.5.

The summary statistics that were obtained from this simulation can be seen in figure 5.6. Overall, the summary statistics from this simulation are similar to experimental data; however, some differences can be noted. The value of the empty space function is slightly below the experimentally observed values for r larger than 20 nm. The biggest difference in the L-function is around $r \in [22, 30]$ nm. This might be because of differences in the sizes of the particles at these length scales. The c-function fits better in the range $r \in [28, 50]$ for this simulation and does not increase as much as for the two other sticking probability functions. The fit of the M-function is also better for this simulation. The biggest difference appears to be for large values of r where the mean cluster size of the simulated structure is slightly smaller than for the STEM data.

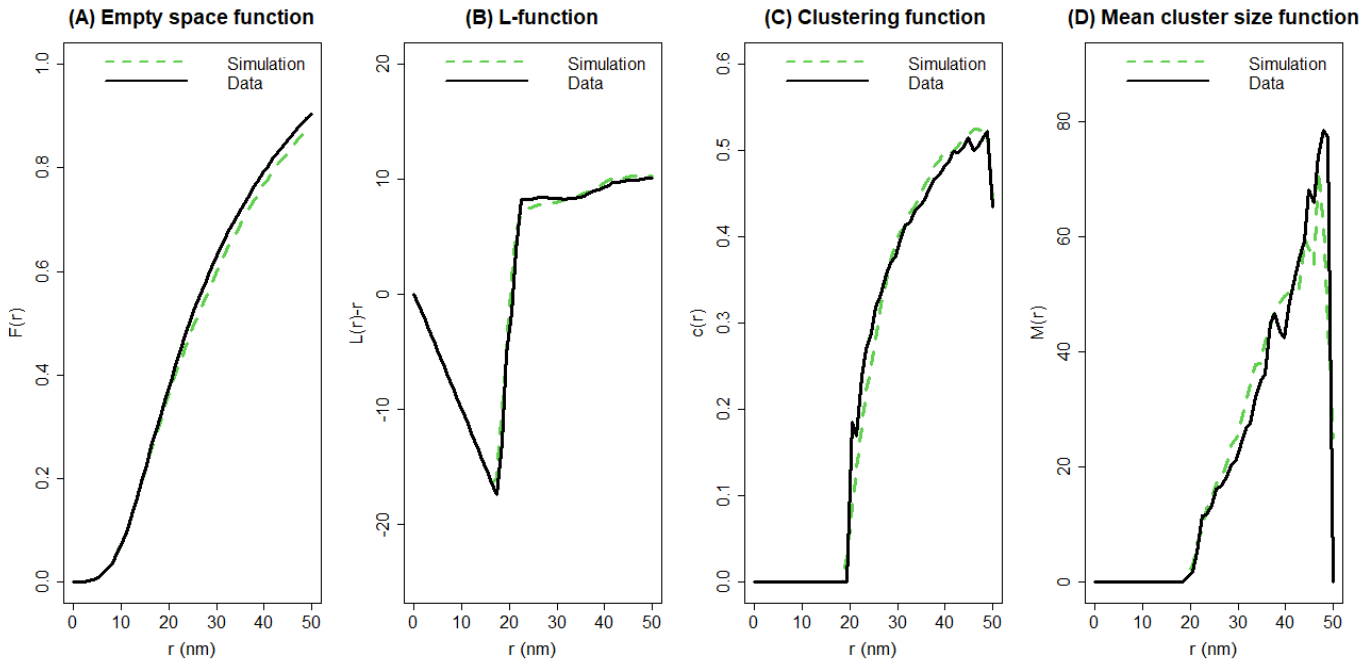


Figure 5.6: Pooled averages for the four summary statistics from simulating with model 3 with $p_0 = 0.0001$, $\delta = 0.001$ and $d = 2.5$, and from the STEM-data (black).

5.1.4 Global envelope tests

As seen in the previous section, the simulation that resulted in the smallest value of S was obtained using a sticking probability as in equation 3.14 with parameters $p_0 = 0.0001$, $\delta = 0.001$ and $s = 2.5$. This model was further analyzed by calculating envelopes with a significance level of $\alpha = 0.01$ for the different summary statistics. The observed summary statistics were taken by averaging the summary statistics over 4 subpatterns in the experimental data as described in section 4.1.3.1. Simulations were then carried out, and 99 averages over 4 subpatterns of the same size as the structures in the observed data were used to compute the envelopes.

The global envelope for the F-function can be seen in figure 5.7. The experimental

curve goes outside the envelope around $r = 7$ and for $r \in [17, 46]$. The null hypothesis is therefore rejected. From the calculated envelope, we can see that overall, the simulated structures give lower values of the empty space function than what is observed in the experimental gel.

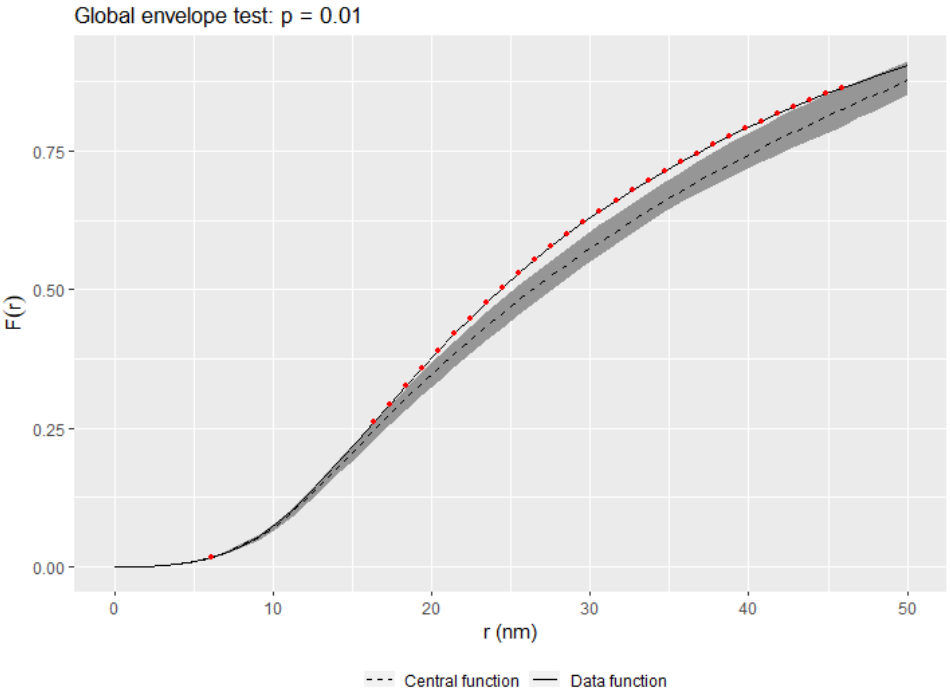


Figure 5.7: Global envelope test for the empty space function. The grey band is the envelope, whereas the dashed line is the central function from the simulations. The black curve corresponds to the STEM data.

The envelope for the L-function in figure 5.8 fits the data quite well, but there are differences around $r \in [18, 22]$. Since the data curve is not entirely inside the envelope, the null hypothesis is rejected. The reason that the curve goes outside of the envelope might be due to differences in the estimated density of the particle diameters and the nearest neighbor distances of the data.

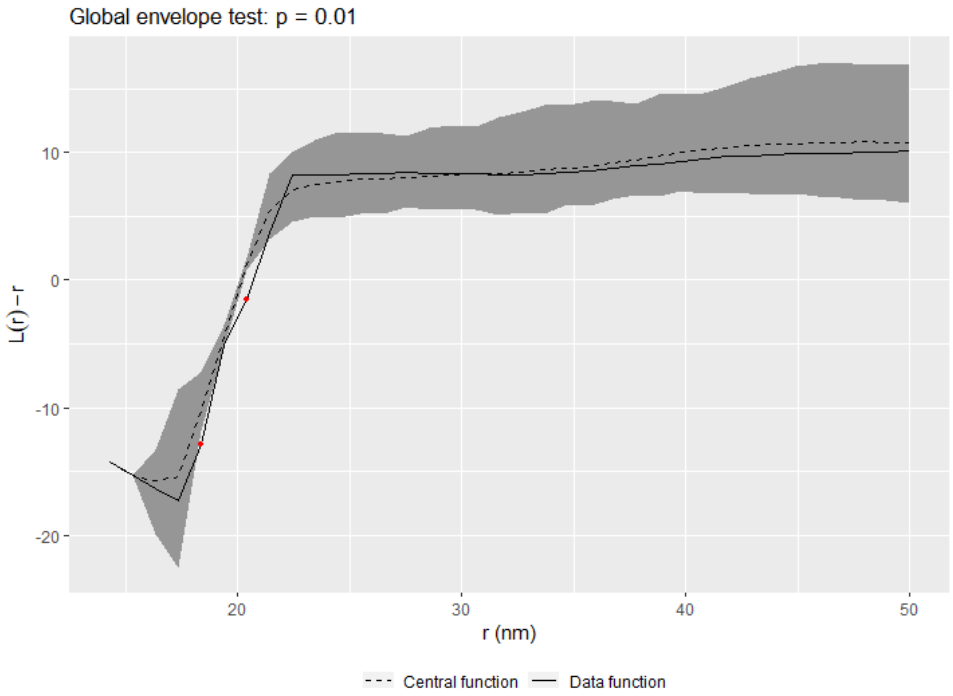


Figure 5.8: Global envelope test for the centered L-function. The black curve corresponds to the STEM data.

Also, the test for the c-function is rejected. Figure 5.9 shows that at lower values of r, the experimental data is more clustered than the simulated structures. However, for r larger than approximately 28 nm, the data function and the central function from the simulations are similar.

The global envelope test for the M-function is also rejected. As shown in figure 5.10, there are differences for small and large values of r. Overall, the M-function is greater for the STEM data than for the simulated gels.

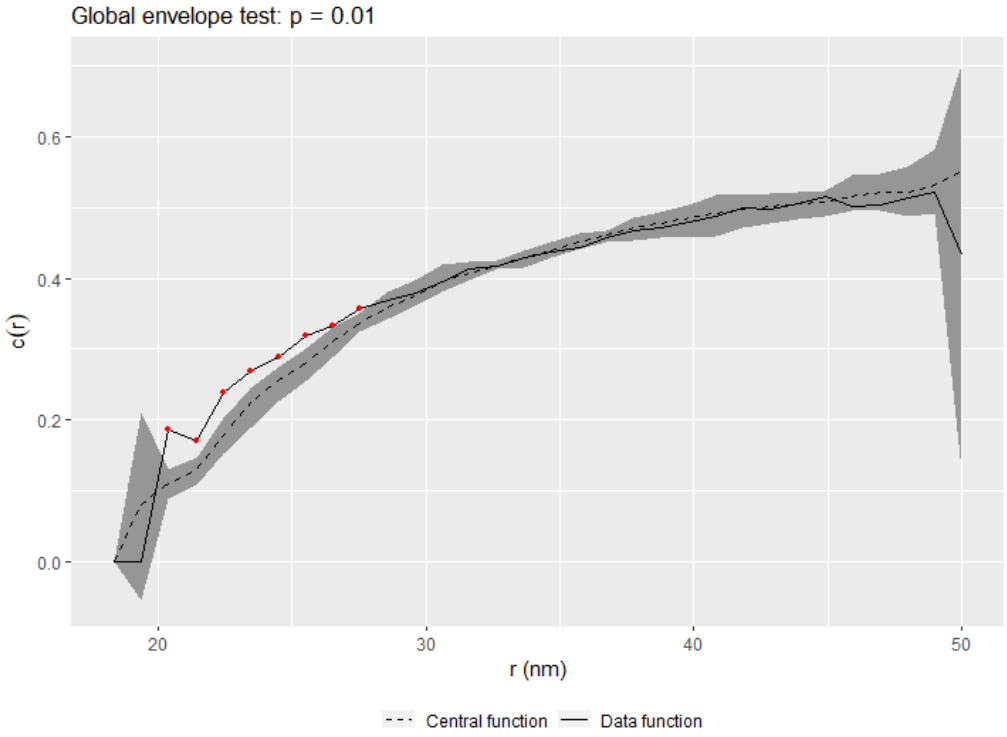


Figure 5.9: Global envelope for the clustering function. The black curve corresponds to the STEM data.

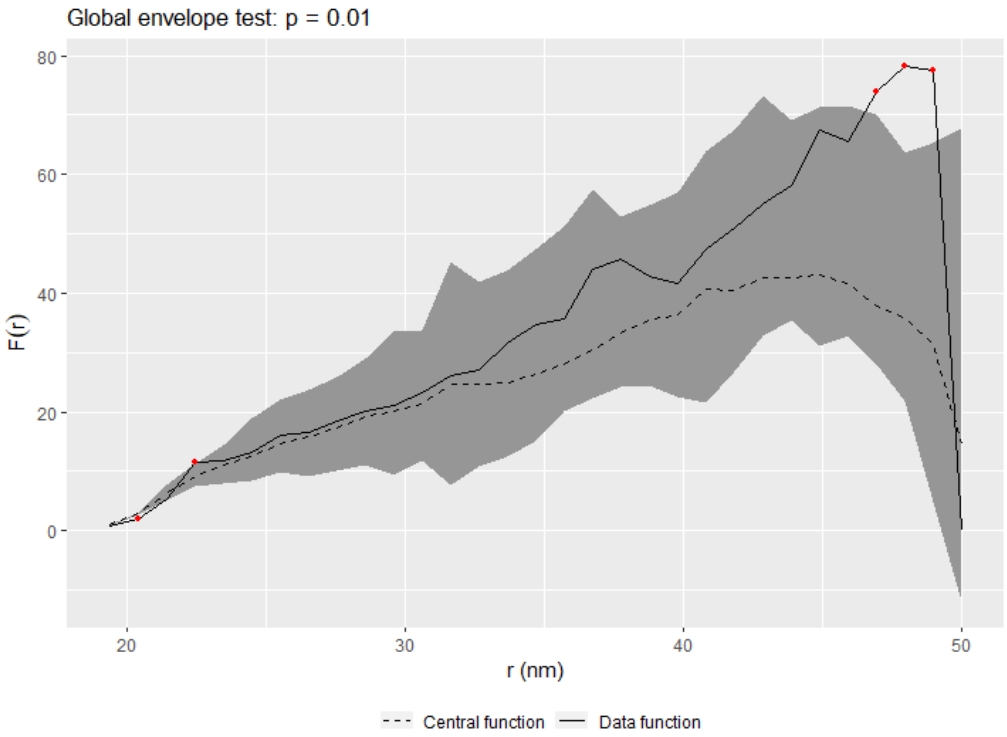


Figure 5.10: Global envelope for the mean cluster size function. The black curve corresponds to the STEM data.

5.2 Fractal dimension

The fractal dimension was estimated by using the random box counting algorithm on a set of boxes of size $\epsilon = [2, 3, 4, 5, 6, 8, 10, 13, 16, 20, 25, 32, 40, 50]$ nm, which are nearly logarithmically distributed. At every length scale, 10^5 boxes with random positions were generated. The fractal dimension was calculated for the experimental data and the simulated structures for every model with the best set of parameters as selected in section 5.1. Since there is no unique way of assigning particle diameters to the experimental structure with data only about the particle centroids, all particles were assumed to have a diameter of 21 nm. The computed values of the fractal dimension for the different aggregates can be seen in table 5.4.

	$D_f \pm \text{SE}$
Data	2.4083 $\pm$0.0459
Model 1, $p = 0.0001$	2.3718 ± 0.0564
Model 2, $p_0 = 0.01$, $\sigma = -0.25$	2.3590 ± 0.0606
Model 3, $p_0 = 0.0001$, $\delta = 0.001$, $d = 2.5$	2.4252 ± 0.0378

Table 5.4: Estimated fractal dimensions D_f with standard error (SE) from linear regression.

All the simulations result in similar values for the fractal dimension; however, the third model gives the closest fractal dimension to the estimated fractal dimension for the physical gel. The fractal dimension for the simulation with model 2 is the furthest from the estimated fractal dimension for the data, but it also has the greatest standard error.

5.3 Mass transport properties

Mass transport simulations were carried out for a structure generated with model 3 with the parameters that gave the smallest value of S. As mentioned earlier, the experimental data had been observed inside a window of size $740 \times 1075 \times 100$ nm^3. Mirror boundary conditions were applied in the directions perpendicular to the flow/diffusion. The size of the structure may impact results, and simulated structures of the same size as the experimental one were therefore generated to make a good comparison. More precisely, a simulation was carried out in a box with periodic boundary conditions of size $740 \times 1075 \times 700$ nm^3 from which 5 structures of size $740 \times 1075 \times 100$ nm^3 were extracted. The particles were assumed to have a diameter of 21 nm.

5.3.1 Flow

Flow simulations were performed in the X- and Y-directions of these boxes, and the calculated permeabilities can be seen in table 5.5. The Reynold's number was smaller than 0.01 for all simulations, and no-slip conditions were used at the material surface.

Flow direction	κ_{data}	$\overline{\kappa}_{\text{sim}}(\kappa_{\text{sim}}^{\text{min}}, \kappa_{\text{sim}}^{\text{max}})$
X	4.76	4.12 (2.96, 5.01)
Y	2.92	5.26 (2.97, 5.31)

Table 5.5: Table of the calculated permeability from flow simulations in two different directions. The average permeability from the 5 simulated structures is denoted by $\overline{\kappa}_{\text{sim}}$, whereas the minimum and maximum out of these permeabilities is denoted by $\kappa_{\text{sim}}^{\text{min}}$ and $\kappa_{\text{sim}}^{\text{max}}$.

From the table above we can see that when calculating the permeability for flow in the X-direction, the value obtained for the physical gel lies between the max and the min of the 5 values from the simulations and is slightly higher than the average permeability from the simulations. When flow is instead simulated in the Y-direction, the permeability from the data falls below the interval from the simulations. However, it is relatively close to the minimum value of the simulations. Figures 5.11 and 5.12 show that the simulated structure seems to have more open passages for flow to pass through, resulting in a higher permeability.

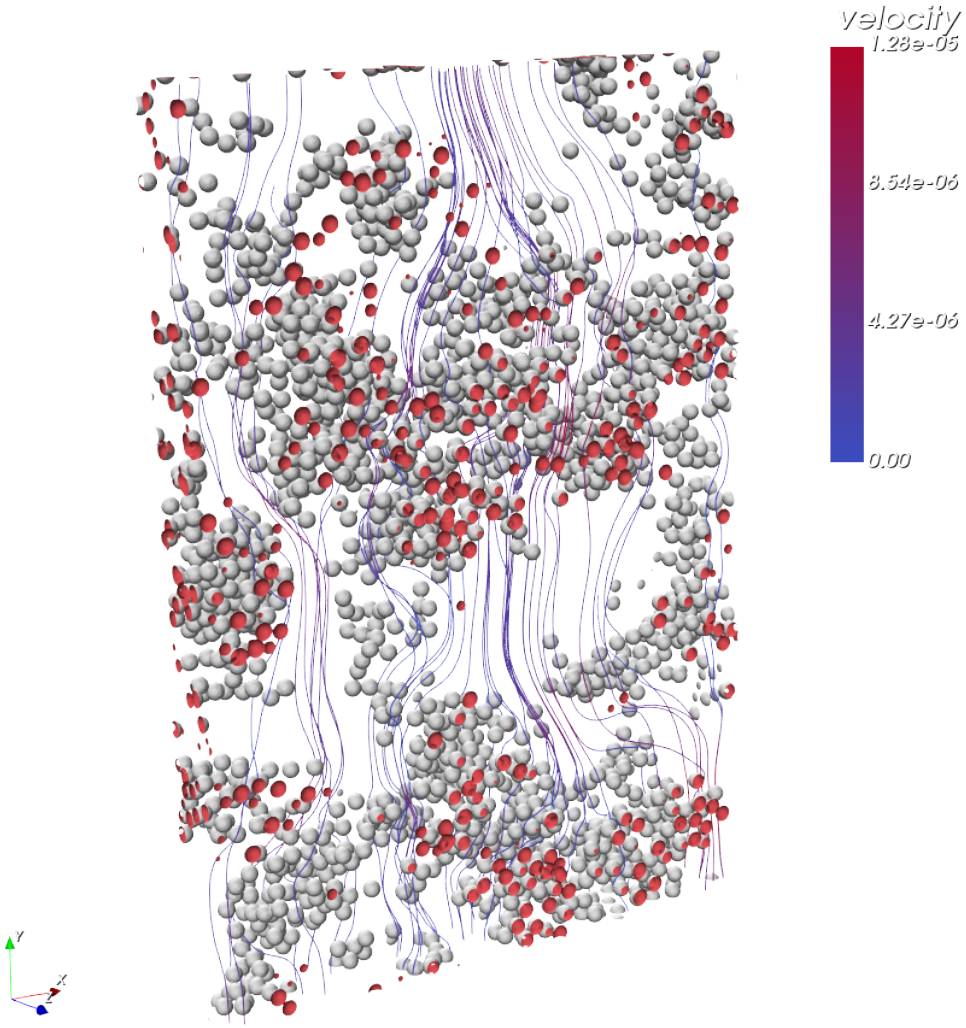


Figure 5.11: Flow simulation for the experimental gel in the Y direction.

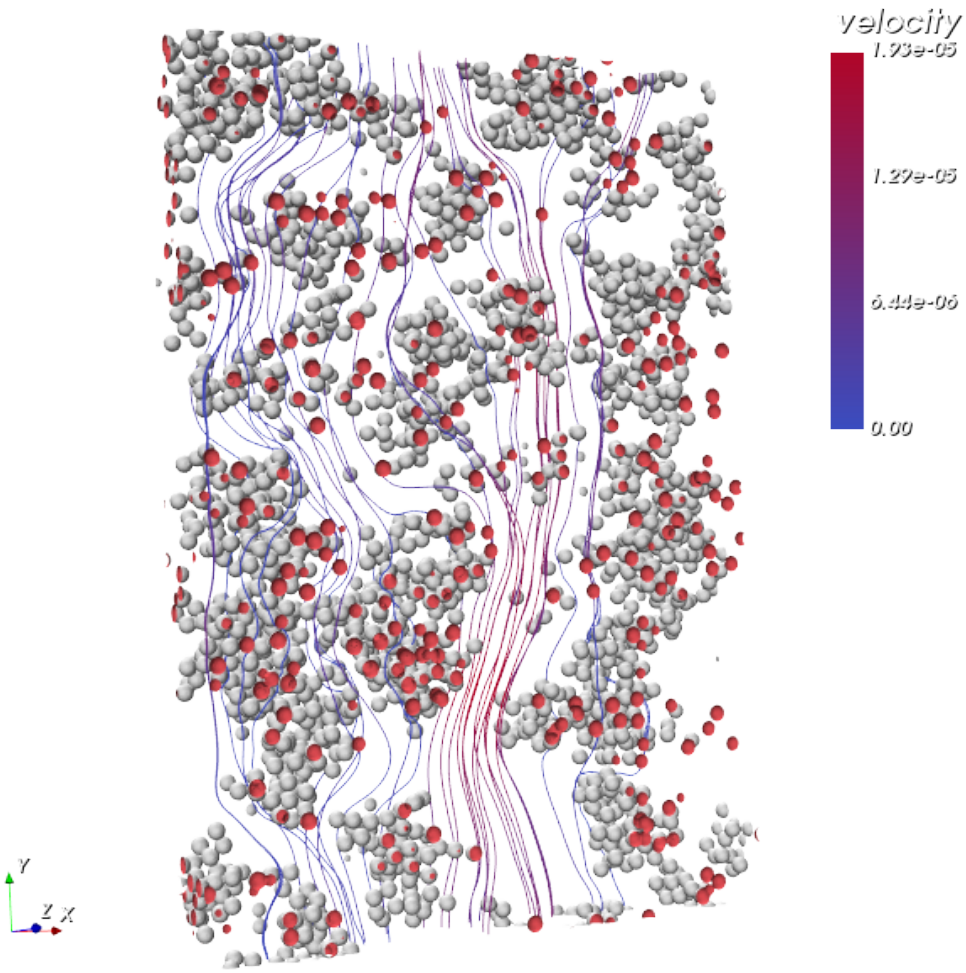


Figure 5.12: Flow simulation in the Y-direction for the gel with permeability closest to the average permeability of the simulated gels.

5.3.2 Diffusion

Diffusion through the materials was simulated for the same structures that had been used for the flow simulations. Neumann (zero flux) boundary conditions were used at the material surface. The geometry factor was calculated to characterize the diffusion through the material, and the obtained results can be found in table 5.6.

Diffusion direction	G_{data}	$\overline{G}_{\text{sim}}(G_{\text{sim}}^{\text{min}}, G_{\text{sim}}^{\text{max}})$
X	0.846	0.846 (0.825, 0.858)
Y	0.844	0.845 (0.823, 0.8596)

Table 5.6: The geometry factor from the diffusion simulations in two different directions. The average of the geometry factor from the 5 simulated structures is denoted by $\overline{G}_{\text{sim}}$, whereas the minimum and maximum out is denoted by $G_{\text{sim}}^{\text{min}}$ and $G_{\text{sim}}^{\text{max}}$.

The geometry factor is very similar for the experimental data and the simulations. The experimental value is close to the mean of the simulations in both directions and lies between the minimum and maximum values from the simulations.

6

Conclusions and suggestions for further research

In this thesis, different functions for the sticking probability in DLCA and RLCA simulations have been investigated. The sticking probabilities used in this study have been assumed to be either constant, mass-dependent, or dependent on the number of particles close to the collision. Post-aggregated structures from simulations and from an experimental gel were compared by analyzing summary statistics from point process theory, fractal scaling, and mass transport properties.

From comparing the goodness-of-fit of the spatial summary statistics, the best results were obtained using model 3 with parameters $p_0 = 0.0001$, $\delta = 0.001$ and $s = 2.5$. Global envelope tests were carried out with this model, and it was seen that even though the summary statistics are similar to the experimental data, there are also systematic differences for all summary statistics. However, the neighbor-dependent sticking probability still gave considerably better results than a constant sticking probability in terms of the summary statistics.

For model 2, all simulations with a negative value of σ improved the sum of squares of the summary statistics compared to using a constant sticking probability with the value of p_0. This suggests that the sticking probability decreases as clusters grow larger; however, both the F-and L-function deviates considerably for the best simulation using this model. In addition, the goodness-of-fit using model 3 was significantly better than for model 2, in which all of the summary statistics fit the experimental data relatively well.

The fractal dimension was calculated for the three models for the sticking probability with the parameters that had resulted in the smallest total sum of squares of the summary statistics. All three models gave fractal dimensions that were similar to the experimental gel. However, the fractal dimension for model 3 was closest to the fractal dimension of the real gel. In most studies, the fractal dimension of structures formed by RLCA lies around 1.9-2.1. The reason why larger values have been obtained in this project is probably due to the relatively high volume fraction of silica particles.

Flow and diffusion were simulated for the experimental data and structures obtained using model 3 with the parameters that gave the smallest sum of squares of the summary statistics. Due to time restrictions, flow and diffusion were not inves-

tigated for structures formed with models 1 and 2. Some differences were found in the flow simulations, but overall, the permeabilities were relatively similar for the experimental and simulated structures. From the diffusion simulations, it was found that the geometry factor from the diffusion simulations was very similar for the experimental and simulated gels. This is reasonable since the geometry factor mainly depends on the volume fraction accessible to diffusion. Since the concentration of primary particles used in the simulations was estimated from the experimental data, the volume fraction is expected to be similar for the experimental and simulated materials. The permeability is instead highly dependent on the presence of wider channels in the material for flow to pass through, which is expected to vary more, especially since the structures investigated were relatively small.

The best results overall were obtained using model 3, which suggests that interaction with other nearby particles is important to describe the aggregation dynamics. The constructed sticking probability might be interpreted as similar to describing pairwise interaction of particles with square well potentials. Interestingly enough, in Häbel *et al.* (2019), parameters of square well potentials were fitted from simulations of static Gibbs point processes with an energy function based on pairwise interaction. In that study, the jump points of the square well potential were obtained to be at 18.27 (being the smallest diameter of a particle in the simulation) and 22.5 nm. Interaction of particles with centroids at a distance up to 22.5 nm is similar to the results in this study, as the best value of s was found to be 2.5 nm, and the average diameter of particles is between 20-21 nm.

Since only a few values for the parameters of the different sticking probabilities have been tested in this study, there is still a possibility that the other models of the sticking probability could have given better results if different values had been used. In addition, even though roughly the same number of values have been tested (between 3 - 5 values of every parameter), the total number of simulations with the different models has been quite different when comparing the total sum of squares since more combinations of parameters have been tested for model 3.

For model 1, the sum of squares of the summary statistics decreased with using smaller sticking probabilities between $p = 0.1$ and $p = 0.0001$. It is, therefore, possible that using even smaller sticking probabilities could have improved the result further. It can also be interesting to investigate parameter values of model 2 further. In a study by Family *et al.* (1985) the Smoluchowski coagulation in equation 3.6 was solved for the mass-dependent sticking probability, and it was found that the development of the cluster size distribution $n(m, t)$ changed in non-trivial ways for different values of σ in equation 3.12 [14]. For instance, it was found that around $\sigma = -0.8$ the distribution $n(m, t)$ changes from a monotonically decreasing function to a bell-shaped curve. Since such small values of σ were disregarded in this study, it might be interesting for further research.

The results might have been affected by the weighted average of the subpatterns taken in equation 4.25. This weighted average of the summary statistics is based

on the idea that subpatterns with more points contain more information about the summary statistics. Even though this might be reasonable for some of the summary statistics, one could, for instance, question this procedure for the F-function, where subpatterns with a lot of emptiness might also be seen as important. However, some tests were done with simple averaging, and the results did not change much since most subpatterns contained roughly the same number of points.

Another possibility for improvement can be to make the dynamics of the aggregation simulations more realistic by including effects from rearrangement of particles due to bond breakage or rotational rearrangement. In addition, gravitational effects and rotational diffusion could also be interesting to include.

This work has suggested that interaction with several particles is important for describing the aggregation dynamics. The model that has been used in this project is rather simplistic, and although there is value in its simplicity and the small number of parameters, it might also be interesting to create more complex models. Since this study's best sticking probability model was similar to the fitted potential functions for the same data, one might try to take inspiration from more accurate potential functions that better describe the interaction between particles in future research.

Bibliography

[1] H. Häbel, A. Särkkä, M. Rudemo, C. H. Blomqvist, E. Olsson, and M. Nordin, "Colloidal particle aggregation in three dimensions", *Journal of Microscopy*, vol. 275, no. 3, pp. 149–158, 2019. DOI: https://doi.org/10.1111/jmi.12823. eprint: https://onlinelibrary.wiley.com/doi/pdf/10.1111/jmi.12823. [Online]. Available: https://onlinelibrary.wiley.com/doi/abs/10.1111/jmi.12823.

[2] L. Köllerström, "Spatial modeling of formation of gel", 2020.

[3] C. Sögaard, "From silica nano-particles to silica gels and beyond - salt induced aggregation of silica nano-particles and the stability of resultant gels", 2020.

[4] C. Hamngren Blomqvist, C. Abrahamsson, T. Gebäck, A. Altskär, A.-M. Hermansson, M. Nydén, S. Gustafsson, N. Lorén, and E. Olsson, "Pore size effects on convective flow and diffusion through nanoporous silica gels", *Colloids and Surfaces A: Physicochemical and Engineering Aspects*, vol. 484, pp. 288–296, 2015, ISSN: 0927-7757. DOI: https://doi.org/10.1016/j.colsurfa.2015.07.032. [Online]. Available: https://www.sciencedirect.com/science/article/pii/S0927775715301102.

[5] T. Björk, *Arbitrage Theory in Continuous Time*. 1999.

[6] M. Longfils, *Quantitative Methods for Diffusion Measurements in Fluorescence Microscopy*. Chalmers University of Technology, 2019.

[7] H. Bergna and W. Roberts, *Colloidal Silica: Fundamentals and Applications*. Jan. 2005, ISBN: ISBN 9780824709679.

[8] J. Mahanty and D. W. Ninham, *Dispersion Forces*. Academic Press: New York, 1979, ISBN: ISBN 9780824709679.

[9] M. Deaconu and E. Tanré, "Smoluchowski's coagulation equation : Probabilistic interpretation of solutions for constant, additive and multiplicative kernels", *Annali della Scuola Normale Superiore di Pisa - Classe di Scienze*, vol. Ser. 4, 29, no. 3, pp. 549–579, 2000. [Online]. Available: http://www.numdam.org/item/ASNSP_2000_4_29_3_549_0/.

[10] R. Pashminehazar, A. Kharaghani, and E. Tsotsas, "Determination of fractal dimension and prefactor of agglomerates with irregular structure", *Powder Technology*, vol. 343, pp. 765–774, 2019, ISSN: 0032-5910. DOI: https://doi.org/10.1016/j.powtec.2018.10.046. [Online]. Available: https://www.sciencedirect.com/science/article/pii/S0032591018308908.

[11] A. González, M. Lach-Hab, and E. Blaisten-Barojas, "On the concentration dependence of the cluster fractal dimension in colloidal aggregation", *Journal of Sol-Gel Science and Technology*, vol. 15, pp. 119–127, Aug. 1999. DOI: 10.1023/A:1008783320920.

[12] P. G. de Gennes, *Scaling Concepts in Polymer Physics*. Ithaca, NY: Cornell University Press, 1979.

[13] B. W. Silverman, *Density Estimation for Statistics and Data Analysis*. London: Chapman & Hall, 1986.

[14] F. Family, P. Meakin, and T. Vicsek, "Cluster size distribution in chemically controlled cluster–cluster aggregation", *The Journal of Chemical Physics*, vol. 83, no. 8, pp. 4144–4150, 1985. DOI: 10.1063/1.449079. eprint: https://doi.org/10.1063/1.449079. [Online]. Available: https://doi.org/10.1063/1.449079.

[15] C. Li and H. Xiong, "3d simulation of the cluster–cluster aggregation model", *Computer Physics Communications*, vol. 185, no. 12, pp. 3424–3429, 2014, ISSN: 0010-4655. DOI: https://doi.org/10.1016/j.cpc.2014.08.017. [Online]. Available: https://www.sciencedirect.com/science/article/pii/S0010465514002951.

[16] P. Sandkühler, M. Lattuada, H. Wu, J. Sefcik, and M. Morbidelli, "Further insights into the universality of colloidal aggregation", *Advances in Colloid and Interface Science*, vol. 113, no. 2, pp. 65–83, 2005, ISSN: 0001-8686. DOI: https://doi.org/10.1016/j.cis.2004.12.001. [Online]. Available: https://www.sciencedirect.com/science/article/pii/S0001868604001095.

[17] D. Stoyan, W. Kendall, S. Chiu, and J. Mecke, *Stochastic Geometry and Its Applications*, ser. Wiley Series in Probability and Statistics. Wiley, 2013, ISBN: 9781118658246. [Online]. Available: https://books.google.se/books?id=GCRI8Q-RUEkC.

[18] H. Häbel, *From experiments with images to 3D models*. Chalmers University of Technology, 2017.

[19] A. Baddeley and R. D. Gill, "Kaplan-meier estimators of distance distributions for spatial point processes", *The Annals of Statistics*, vol. 25, no. 1, pp. 263–292, 1997, ISSN: 00905364. [Online]. Available: http://www.jstor.org/stable/2242720 (visited on 09/06/2022).

[20] T. Rajala, "Spatial point processes and graph based statistical features", 2010.

[21] C. Redenbach and A. Särkkä, "Parameter estimation for growth interaction processes using spatio-temporal information", *Computational Statistics Data Analysis*, vol. 57, no. 1, 2013. DOI: https://doi.org/10.1016/j.csda.2012.08.006. [Online]. Available: https://www.sciencedirect.com/science/article/pii/S016794731200309X.

[22] M. Myllymäki, T. Mrkvička, P. Grabarnik, H. Seijo, and U. Hahn, "Global envelope tests for spatial processes", *Journal of the Royal Statistical Society: Series B (Statistical Methodology)*, vol. 79, no. 2, pp. 381–404, Mar. 2016. DOI: 10.1111/rssb.12172. [Online]. Available: https://doi.org/10.1111%2Frssb.12172.

[23] "A simplified monte carlo significance test procedure", vol. 30, no. 3, pp. 582–598, 1968, ISSN: 00359246. [Online]. Available: http://www.jstor.org/stable/2984263 (visited on 08/11/2022).

[24] P. Diggle, "Statistical analysis of spatial and spatio-temporal point patterns", Jan. 2013.

[25] R. M. Péter Tamás Kovács Marcell Nagy, "Comparative analysis of box-covering algorithms for fractal networks", *Applied Network Science*, 2021. DOI: https://doi.org/10.1007/s41109-021-00410-6.

[26] M. Wozniak, F. Onofri, S. Barbosa, J. Yon, and J. Mroczka, "Comparison of methods to derive morphological parameters of multi-fractal samples of particle aggregates from tem images", *Journal of Aerosol Science*, vol. 47, pp. 12–26, 2012, ISSN: 0021-8502. DOI: https://doi.org/10.1016/j.jaerosci.2011.12.008. [Online]. Available: https://www.sciencedirect.com/science/article/pii/S0021850211001984.

[27] A. Atangana, "Chapter 2 - principle of groundwater flow", in *Fractional Operators with Constant and Variable Order with Application to Geo-Hydrology*, A. Atangana, Ed., Academic Press, 2018, pp. 15–47, ISBN: 978-0-12-809670-3. DOI: https://doi.org/10.1016/B978-0-12-809670-3.00002-3. [Online]. Available: https://www.sciencedirect.com/science/article/pii/B9780128096703000023.

[28] E. Jacops, M. Aertsens, N. Maes, C. Bruggeman, S. Rudy, B. Krooss, A. Amann, and R. Littke, "The dependency of diffusion coefficients and geometric factor on the size of the diffusing molecule: Observations for different clay-based materials", *Geofluids*, vol. 2017, pp. 1–16, Dec. 2017. DOI: 10.1155/2017/8652560.

[29] T. Gebäck and A. Heintz, "A lattice boltzmann method for the advection-diffusion equation with neumann boundary conditions", *Commun. Comput. Phys.*, vol. 15, pp. 487–505, Feb. 2014. DOI: 10.4208/cicp.161112.230713a.

DEPARTMENT OF SOME SUBJECT OR TECHNOLOGY
CHALMERS UNIVERSITY OF TECHNOLOGY
Gothenburg, Sweden
www.chalmers.se



CHALMERS
UNIVERSITY OF TECHNOLOGY